Volume 7, Issue 13 – January – June - 2023

ECORFAN

Journal- Taiwan

ISSN-On line 2524-2121

ECORFAN®

ECORFAN Journal-Taiwan, Volume 7, Issue 13, January - June 2023, is a journal edited semestral by ECORFAN. Taiwan, Taipei. YongHe district, Zhong Xin, Street 69. Postcode: 23445. WEB: www.ecorfan.org/taiwan/journal@ecorfan.org. Editor in Chief: VARGAS-DELGADO, Oscar. PhD. ISSN: 2524-2121. Responsible for the latest update of this number ECORFAN Computer Unit. ESCAMILLA-BOUCHÁN, Imelda. PhD, LUNA-SOTO, Vladimir. PhD, last updated June 30, 2023.

ECORFAN Journal- Taiwan

Definition of Journal

Scientific Objectives

Support the international scientific community in its written production Science, Technology and Innovation in the Field of Physical Sciences Mathematics and Earth sciences, in Subdisciplines of optical astronomy, optical characterization, optical encoder, experimental research, planetary magnetic fields, ultraviolet radiation, lasers, algorithms and optical waves.

ECORFAN-Mexico SC is a Scientific and Technological Company in contribution to the Human Resource training focused on the continuity in the critical analysis of International Research and is attached to CONAHCYT-RENIECYT number 1702902, its commitment is to disseminate research and contributions of the International Scientific Community, academic institutions, agencies and entities of the public and private sectors and contribute to the linking of researchers who carry out scientific activities, technological developments and training of specialized human resources with governments, companies and social organizations.

Encourage the interlocution of the International Scientific Community with other Study Centers in Mexico and abroad and promote a wide incorporation of academics, specialists and researchers to the publication in Science Structures of Autonomous Universities - State Public Universities - Federal IES - Polytechnic Universities - Technological Universities - Federal Technological Institutes - Normal Schools - Decentralized Technological Institutes - Intercultural Universities - S & T Councils - CONAHCYT Research Centers.

Scope, Coverage and Audience

ECORFAN Journal- Taiwan is a Journal edited by ECORFAN-Mexico S.C in its Holding with repository in Taiwan, is a scientific publication arbitrated and indexed with semester periods. It supports a wide range of contents that are evaluated by academic peers by the Double-Blind method, around subjects related to the theory and practice of optical astronomy, optical characterization, optical encoder, experimental research, planetary magnetic fields, ultraviolet radiation, lasers, algorithms and optical waves with diverse approaches and perspectives , That contribute to the diffusion of the development of Science Technology and Innovation that allow the arguments related to the decision making and influence in the formulation of international policies in the Field of Physical Sciences Mathematics and Earth sciences. The editorial horizon of ECORFAN-Mexico® extends beyond the academy and integrates other segments of research and analysis outside the scope, as long as they meet the requirements of rigorous argumentative and scientific, as well as addressing issues of general and current interest of the International Scientific Society.

Editorial Board

Arbitration Committee

Assignment of Rights

The sending of an Article to ECORFAN Journal- Taiwan emanates the commitment of the author not to submit it simultaneously to the consideration of other series publications for it must complement the Originality Format for its Article.

The authors sign the Authorization Format for their Article to be disseminated by means that ECORFAN-Mexico, S.C. In its Holding Taiwan considers pertinent for disclosure and diffusion of its Article its Rights of Work.

Declaration of Authorship

Indicate the Name of Author and Coauthors at most in the participation of the Article and indicate in extensive the Institutional Affiliation indicating the Department.

Identify the Name of Author and Coauthors at most with the CVU Scholarship Number-PNPC or SNI-CONAHCYT- Indicating the Researcher Level and their Google Scholar Profile to verify their Citation Level and H index.

Identify the Name of Author and Coauthors at most in the Science and Technology Profiles widely accepted by the International Scientific Community ORC ID - Researcher ID Thomson - arXiv Author ID - PubMed Author ID - Open ID respectively.

Indicate the contact for correspondence to the Author (Mail and Telephone) and indicate the Researcher who contributes as the first Author of the Article.

Plagiarism Detection

All Articles will be tested by plagiarism software PLAGSCAN if a plagiarism level is detected Positive will not be sent to arbitration and will be rescinded of the reception of the Article notifying the Authors responsible, claiming that academic plagiarism is criminalized in the Penal Code.

Arbitration Process

All Articles will be evaluated by academic peers by the Double Blind method, the Arbitration Approval is a requirement for the Editorial Board to make a final decision that will be final in all cases. MARVID® is a derivative brand of ECORFAN® specialized in providing the expert evaluators all of them with Doctorate degree and distinction of International Researchers in the respective Councils of Science and Technology the counterpart of CONAHCYT for the chapters of America-Europe-Asia- Africa and Oceania. The identification of the authorship should only appear on a first removable page, in order to ensure that the Arbitration process is anonymous and covers the following stages: Identification of the Journal with its author occupation rate - Identification of Authors and Coauthors - Detection of plagiarism PLAGSCAN - Review of Formats of Authorization and Originality-Allocation to the Editorial Board-Allocation of the pair of Expert Arbitrators-Notification of Arbitration -Declaration of observations to the Author-Verification of Article Modified for Editing-Publication.

Instructions for Scientific, Technological and Innovation Publication

Knowledge Area

The works must be unpublished and refer to topics of optical astronomy, optical characterization, optical encoder, experimental research, planetary magnetic fields, ultraviolet radiation, lasers, algorithms and optical waves and other topics related to Physical Sciences Mathematics and Earth sciences.

Presentation of the content

In the first article we present, *Switchable emissions of an Erbium-doped fiber laser using cascaded MZIs based on CHCF* by HERRERA-PIAD, Luis, VELAZQUEZ-GONZALEZ, Felipe, DURAN-PEREZ, Oscar and BRIANZA-GORDILLO, Gerardo, with adscription in the Universidad Tecnológica de Aguascalientes, in the next article we present, *Identification of an instrumental proposal based on fiber optic sensors of the Bragg grating type for implementation in an experimental platform for dynamic analysis* by HERNÁNDEZ-GONZÁLEZ, Josué Iván, TORRES-CEDILLO, Sergio Guillermo, HERNÁNDEZ-MORENO, Hilario and CORTÉS-PÉREZ, Jacinto, with adscription in the Instituto Politécnico Nacional and Universidad Nacional Autónoma de México, in the next article we present, *Comparative study of the effects caused by polymers, bubbles and surfactants in a turbulent flow* by LÓPEZ AGUADO-MONTES, José Luis, RIVERA-LÓPEZ, Jesús Eduardo, ARCINIEGA-MARTÍNEZ, José Luis and JUAREZ-NAVARRO, Carlos Alfonso, with adscription in the Instituto Politécnico Nacional, in the last article we present, *Comparison and interpretation of solarimetric station data (diffuse solar radiation, UVB radiation, temperature, and relative humidity) from January 2017 to November 2018 in Zacatecas* by BERLANGA-MORENO, Edgar Darío, GARCÍA-GONZÁLEZ, Juan Manuel, GONZÁLEZ-CABRERA, Adriana Elizabeth and VILLEGAS-MARTÍNEZ, Rodrigo Cervando, with adscription in the Universidad Autónoma de Zacatecas.

Content

Article **ECORFAN Journal- Taiwan**
June, 2023 Vol.7 No.13 1-6

Switchable emissions of an Erbium-doped fiber laser using cascaded MZIs based on CHCF

Emisiones conmutables de un láser de fibra dopada con Erbio utilizando MZIs en cascada basados en CHCF

HERRERA-PIAD, Luis†*, VELAZQUEZ-GONZALEZ, Felipe, DURAN-PEREZ, Oscar and BRIANZA-GORDILLO, Gerardo

Universidad Tecnológica de Aguascalientes, CICMA, Mechatronics Department, Blvrd Juan Pablo II, Aguascalientes 20200, México

ID 1st Author: *Luis, Herrera-Piad* / **ORC ID**: 0000-0002-6204-0193, **CVU CONAHCYT ID**: 546217

ID 1st Co-author: *Felipe, Velazquez-Gonzalez* / **ORC ID**: 0009-0002-2129-7643

ID 2nd Co-author: *Oscar, Duran-Perez* / **ORC ID**: 0009-0007-7084-7556, **CVU CONAHCYT ID**: 238023

ID 3rd Co-author: *Gerardo, Brianza-Gordillo*/ **ORC ID**: 0000-0002-9384-643X, **CVU CONAHCYT ID**: 668961

DOI: 10.35429/EJT.2023.13.7.1.6 Received March 20, 2023; Accepted June 30, 2023

Abstract

In this work, a single and dual-wavelength erbium-doped fiber laser (EDFL) based on two Mach-Zehnder interferometers (MZIs) in cascade structure was experimentally validated. MZIs were assembled by joining a capillary hollow-core fiber (CHCF) piece between two multimode fibers (MMFs) sections. The switchable operation is reached by moving the spectrum of one MZI when the temperature is increased. The maximum measured signal noise to ratio (SNR) was more than 50 dB for the single and dual-wavelength laser lines. Besides, stable output is shown since no power and wavelength variations were noticed. It is important to mention that emissions are obtained at precise wavelength positions and not arbitrarily as described by other investigations. This EDFL can be used in applications of optical fiber communications systems and fiber sensing.

Erbium-doped fiber laser, Mach-Zehnder interferometer, Multiwavelength laser emission

Resumen

En este trabajo, se validó experimentalmente un láser de fibra dopada con erbio (EDFL) con emisión simple y dual, basado en dos interferómetros Mach-Zehnder (MZI) en cascada. Los MZI se ensamblaron uniendo una pieza de fibra de núcleo hueco capilar (CHCF) entre dos secciones de fibras multimodo (MMF). La operación conmutable se logra desplazando el espectro de un MZI cuando se aumenta la temperatura. El valor máximo medido de relación señal a ruido (SNR) fue de más de 50 dB. Además, se muestra una salida estable ya que no se observaron variaciones de potencia ni de longitud de onda. Es importante mencionar que las emisiones se obtienen en posiciones de longitud de onda precisas y no de manera arbitraria como lo describen otras investigaciones. Este EDFL se puede utilizar en aplicaciones de sistemas de comunicaciones de fibra óptica y sensores.

Láser de fibra dopada con erbio, Interferómetro Mach-Zehnder, Emisión múltiple

Citation: HERRERA-PIAD, Luis, VELAZQUEZ-GONZALEZ, Felipe, DURAN-PEREZ, Oscar and BRIANZA-GORDILLO, Gerardo. Switchable emissions of an Erbium-doped fiber laser using cascaded MZIs based on CHCF. ECORFAN Journal-Taiwan. 2023. 7-13: 1-6

* Author correspondence (e-mail: luis.piad@utags.edu.mx)
† Researcher contributing as first author.

Introduction

Multiwavelength erbium-doped fiber lasers (EDFLs) are used for different applications like wavelength division multiplexing [1], [2], optical fiber sensing [3], [4], and microwave photonics [5], [6]. In this kind of lasers, unstable emissions is commonly appreciated [7–9]. Several optical fiber structures have been implemented to fabricate interferometers for this lasers. Y. Lv *et al*. [10] recommended a Mach-Zehnder interferometer (MZI) with a triple-core pho-tonic crystal fiber to obtain single, dual and triple-wavelength EDFL.

The side-mode suppression ratio (SMSR) was 50, 45, and 37 dB for single, dual, and triple-wavelength emission, respectively, and the 3 dB linewidth was 0.026 nm. The power fluctuations for single, dual, and triple-wavelength emissions were 0.44, 0.77, and 0.96 dB, respectively. Y. Qi *et al*. [11] proposed a switchable single, dual, and triple-wavelength EDFL, depending on a MZI using the core-offset technique with 57 cm of few-mode fiber between two single-mode fibers (). A signal-noise ratio (SNR) of 54, 43, and 49 dB for single, dual, and triple-wavelength emission respectively, was presented, and the 3 dB linewidth was 0.02 nm. The power variations for single, dual, and triple-wavelength emissions were 1.14, 2, and 4.33 dB, respectively. For the mentioned works, the multiwavelength lasing operation was accomplished by changing the polarization controller (PC) positions. This method requires a lot of time and shows lack of control of emissions.

Alternatively, other investigations use two filters in cascade to achieve multiwavelength laser emissions [12–16]. Z. Tang *et al*. [12] proposed two MZIs to obatain a single and dual-wavelength laser. One of the MZI was fabricated by splicing a piece of a photonic crystal fiber between two SMF, the second one uses two conventional fiber couplers. The reported SMSR was of 45 and 42 dB for single and dual-wavelength emissions, respectively, and the measured 3 dB linewidths of the single and dual-wavelength emissions were 0.026 and 0.03 nm, respectively. One disadvantage of these works is the assemblage of MZI with couplers, making the setup huger.

In this work, a stable single and dual-wavelength EDFL based on two cascaded MZIs was offered and experimentally validated. The MZIs were fabricated by splicing a piece of capillary hollow core fiber (CHCF) between two sections of multimode fibers (MMF). The maximum length of these MZIs was 5 mm, making these devices attractive because of their simple fabrication, small size and low cost. The MZI with larger FSR was used as wavelength chooser, and the other MZI controls the separation of the switchable emissions.

The innovation of this single and dual-wavelength EDFL is that the switchable operation is accomplished by thermally moving the interference pattern of one MZI and not by changing the polarization state like the examples cited before. This setup offers an easy method to switch emissions over predicted wavelength positions, removing the unpredictability through polarization tuning. The maximum value of SNR was 58.9 dB for the single and dual-wavelength laser emissions, and the linewidth was 30 pm. Furthermore, no power and wavelength variations were identified during the single and dual-wavelength operation.

1. Content

As presented in Figure 1, a fiber ring laser was assembled, where a laser diode launched light to a 980/1550 wavelength division multiplexer (WDM) fiber coupler. A section of 4 m of EDF was utilized as the gain medium, a PC and an isolator were added to the cavity to achieve an enhanced SNR and to operate in a unidirectional way, respectively. An optical fiber coupler (90/10) allowed to observe the output, where the 10% port was linked to optical spectrum analyzer (OSA), and the 90% port was used to close the cavity for continuous laser generation. Additionally, the two MZIs were positioned into the cavity.

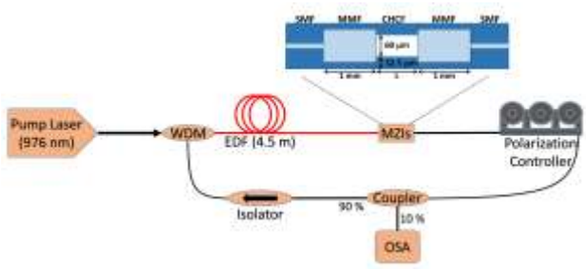

Figure 1 Experimental setup of the fiber ring laser

ISSN 2524-2121

1.1 Fabrication and working principle

These MZIs consist of splicing a section of CHCF (inner and outer diameters of 62.5 and 125 µm, respectively) between two pieces of 1 mm of MMF (105/125 µm), and this structure was inserted between two standard SMF, see Figure 1. MMF sections work as mode couplers, distributing light to the hollow core and the ring cladding of the CHCF.

Three MZIs where fabricated with different free spectral range (FSR). The execution of this laser involves two MZIs in a cascade structure. One of these devices (MZI1) has an FSR of more than 10 nm, and the other (MZI2) has an FSR of less than 2 nm. For the MZI1, two MZIs were fabricated, and their FSRs are 17.82 and 13.29 nm equivalent to a predictable dimension of 0.3 (MZI1a) and 0.4 mm (MZI1c), respectively (see Figure 2). On the other hand, MZI2 was built with a FSR of 1.8 nm (see Figure 2), corresponding to an estimated length of 3 mm.

It is vital to mention that we reported [18] a tunable erbium-doped fiber ring laser using a MZI based on CHCF, where we prove that the spectral response of the MZI experiences a movement to higher wavelength when the temperature rises with a slope of 33 pm/ ºC. This thermal tunability allows us to combine two MZIs in a fiber ring laser cavity using the MZI1 as a wavelength picker (bigger FSR), and MZI2 is in a stable state. Then, the interference pattern of the MZI1 is moving over the spectrum of the MZI2 to select a peak/s for laser emission. The MZI2 controls the switchable period (FSR =1.8 nm), and the laser linewidth of 0.03 nm for all emissions when the two MZIs are connected in a cascade arrangement.

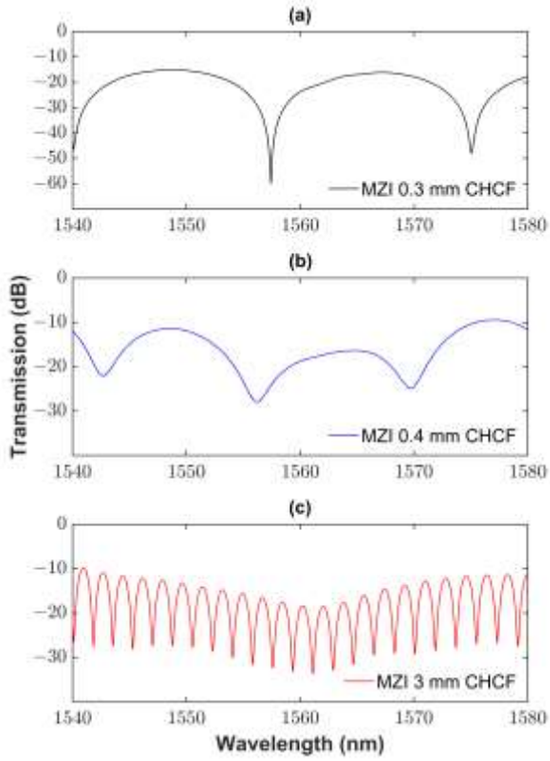

Figure 2 Transmission spectra of (a) MZI1a, (b) MZI1b, (c) MZI2

The spectral responses of the cascade combination of the MZI1a and MZI1b with the MZI2 are shown in Figure 3. For an improved understanding, the peaks with maximum transmission in the interference pattern produced by two cascaded MZIs are marked to specify the high probability to become a laser emission.

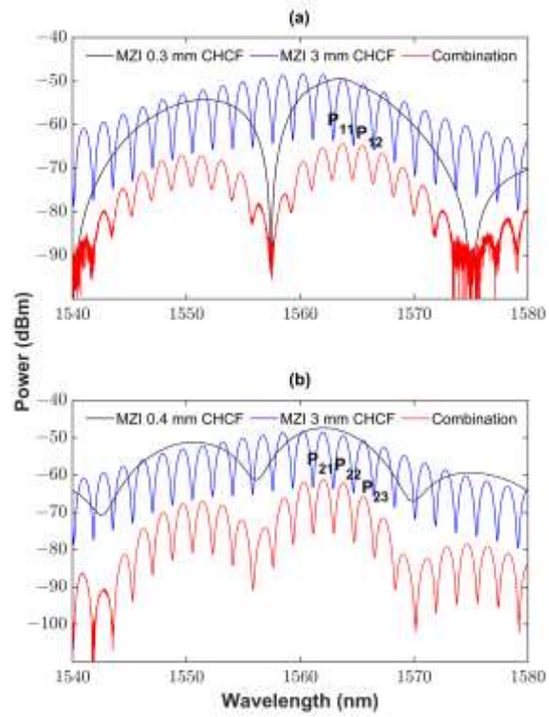

Figure 3 Transmission spectra of the MZI2 linked in sequence with the (a) MZI1a, (b) MZI1b (Cascade configuration)

ISSN 2524-2121

1.2 Results and Discussion

An experimental study was carried out to examine the switchable operation of the EDFL. The MZI2 was placed on a hot plate (Echotherm, Model IC20) at a constant temperature of 20 °C, meanwhile the MZI1 was on another hot plate (Thermo Scientific™, model HP88854100), where the temperature was increased.

The transmission spectrum of the cascaded MZI2 and MZI1a is shown in Figure. 3 (a). Consequently, laser emission will possibly emerge at P11 since this peak shows the maximum transmission. At the beginning, the pump laser current was static at 400 mA, and both interferometers were at 20 ºC, with these conditions, a laser emission at 1563.7 nm is observed (P11) with a SNR of 58.9 dB (see Figure. 4). Then, MZI1a was heated in steps of 1 ºC until to 29 ºC, where laser emission remains immobile. When the MZI1a temperature reached 30 ºC, another laser emission shows up at 1565.5 nm (P12) with a SNR of 58.6 dB. This dual emission is present until the MZI1a reaches a temperature of 40 ºC, where the EDFL changes to one laser emission at P12, remaining fixed from 40 to 160 ºC (see Figure 4). Moreover, the wavelength stability of laser emissions was measured and variations were not detected.

For the second case, the peak P21 shows the highest transmission (see Figure. 3), therefore a laser emission was detected at 1562.7 nm (P21) with a SNR of 50.3 dB (see Figure. 5). An analogous study was carried out, now achieving another two wavelength positions with laser emission, P22 and P23 at 1564.5 and 1566.3 nm with a SNR of 50.9 and 50.8 dB respectively.

The greatest noteworthy characteristic of our EDFL is that it can be switched from single-wavelength laser emission to a dual-wavelength by increasing the temperature of the MZI1, proposing a huge benefit compared with others switchable lasers based on polarization mentioned before. Another advantage is the constant wavelength spacing of 1.8 nm between the emissions, provided by the FSR of the MZI2, showing the controlled way of the achievement of our EDFL emissions.

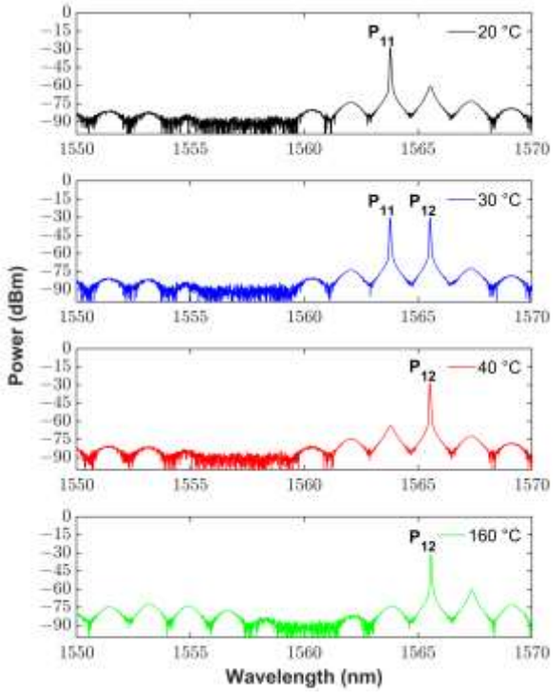

Figure 4 Switchable operation of the EDFL using MZI2 and MZI1a

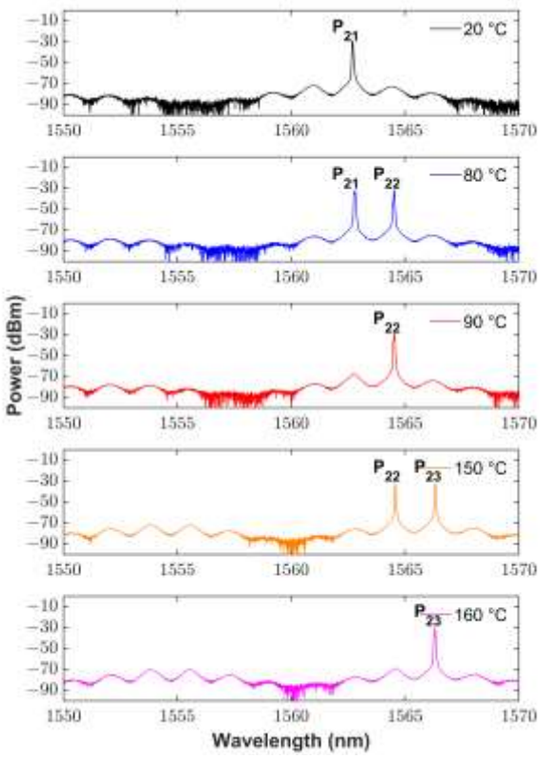

Figure 5 Switchable operation of the EDFL using MZI2 and MZI1b

Conclusions

In this work, a single and dual-wavelength EDFL has been proposed and experimentally verified. The all-fiber MZIs were fabricated by splicing a small piece of capillary hollow core fiber (CHCF) between two segments of MMF.

ISSN 2524-2121

HERRERA-PIAD, Luis, VELAZQUEZ-GONZALEZ, Felipe, DURAN-PEREZ, Oscar and BRIANZA-GORDILLO, Gerardo. Switchable emissions of an Erbium-doped fiber laser using cascaded MZIs based on CHCF. ECORFAN Journal-Taiwan. 2023

These MZIs show good features like easy fabrication, small size, low cost, and robustness. Furthermore, their interference patterns have high fringe contrasts and do not suffer alterations when the input polarization state of light is changed. The MZI with bigger FSR was used as wavelength selector, meanwhile, a MZI with smaller FSR determine the spacing of the switchable step. The innovation of this EDFL is that the switchable operation is accomplished by thermally tuning the interference pattern of the MZI and not by changing the polarization state into the cavity. The maximum SNR was 58.9 dB and no power and wavelength fluctuations were detected. For a future work, the nice performance of this switchable EDFL can be tested in optical fiber communications systems and fiber sensing applications.

Funding

This work has been funded by CONACyT [grant number CB2017-2018-A1-S-31806, CB2016-286368, and CB2016-286629]; in part by UNIVERSIDAD DE GUANAJUATO [grant number CIIC-088/2022].

Referencias

[1] Sang-Mook Lee, Ki-Man Choi, Sil-Gu Mun, Jung-Hyung Moon, Chang-Hee Lee, "Dense WDM-PON based on wave-length-locked Fabry-Perot laser diodes", IEEE Photonics Technol. Lett., 17, pp. 1579–1581, 2005. *https://doi.org/10.1109/LPT.2005.848558*

[2] M.K.S. Al-Mashhadani, T.F. Al-Mashhadani, H.H. Goktas, Broadly tunable 40 GHz Brillouin frequency spacing multiwave-length Brillouin–Erbium fiber laser for DWDM, Opt. Commun., 451, pp. 116–123, 2019. *https://doi.org/10.1016/j.optcom.2019.06.040*

[3] S. Diaz, M. Lopez-Amo, Dual-wavelength single-longitudinal-mode erbium fiber laser for temperature measurements, Opt. Eng., 53, 036106, 2014. *https://doi.org/10.1117/1.OE.53.3.036106*

[4] Y. Li, C. Zhou, J. Tian, S. Ji, Y. Yao, An all-fiber multi-channel ultrasonic sensor using a switchable fiber Bragg gratings filter in erbium-doped fiber laser, J. Light. Technol., 37, pp. 4330–4339, 2019. *https://doi.org/10.1109/JLT.2019.2923645*

[5] N. A. B. Ahmad, S.H. Dahlan, M. H. Jamaluddin, R. Sanchez-Lara, N. A. Cholan, A microwave signal generation technique based on Brillouin-erbium fiber laser, Int. J. Integr. Eng., 11, 2019. *https://doi.org/10.1109/JLT.2019.2923645*

[6] A. Kumar, A. Gautam, V. Priye, Microwave photonic mixer using DP-DDMZM for next generation 5G cellular systems, Fiber Integr. Opt., 39, pp. 149–168, 2020. *https://doi.org/10.1080/01468030.2020.1826068*

[7] D.S. Moon, U.-C. Paek, Y. Chung, Multi-wavelength lasing oscillations in an erbium-doped fiber laser using few-mode fiber Bragg grating, Opt. Express., 12, 6147. 2004. *https://doi.org/10.1364/OPEX.12.006147*

[8] Y. Liu, X. Dong, P. Shum, S. Yuan, G. Kai, X. Dong, Stable room-temperature multi-wavelength lasing realization in ordinary erbium-doped fiber loop lasers, Opt. Express., 14, 9293, 2006. *https://doi.org/10.1364/OE.14.009293*

[9] W.G. Chen, S.Q. Lou, S.C. Feng, L.W. Wang, H.L. Li, T.Y. Guo, S.S. Jian, Switchable multi-wavelength fiber ring laser based on a compact in-fiber Mach-Zehnder interferometer with photonic crystal fiber, Laser Phys., 19, pp. 2115–2119, 2009. *https://doi.org/10.1134/S1054660X09210026*

[10] Y. Lv, S. Lou, Z. Tang, X. Liu, X. Wang, Tunable C-band and L-band multi-wavelength erbium-doped fiber ring laser based on a triple-core photonic crystal fiber with polarization-dependent loss, Opt. Laser Technol., 128, 106269, 2020. *https://doi.org/10.1016/j.optlastec.2020.106269*

[11] Y. Qi, Z. Kang, J. Sun, L. Ma, W. Jin, Y. Lian, S. Jian, Wavelength-switchable fiber laser based on few-mode fiber filter with core-offset structure, Opt. Laser Technol., 81, pp. 26–32, 2016. *https://doi.org/10.1016/j.optlastec.2016.01.022*

[12] Z. Tang, S. Lou, X. Wang, Stable and widely tunable single-/dual-wavelength erbium-doped fiber laser by cascading a twin-core photonic crystal fiber based filter with Mach-Zehnder interferometer, Opt. Laser Technol., 109, pp. 249–255, 2019. *https://doi.org/10.1016/j.optlastec.2018.07.060*

[13] W. He, H. Yuan, X. Lou, L. Zhu, M. Dong, Multi-wavelength switchable erbium-doped fiber laser based on a hybrid filter incorporating a bi-tapered Mach–Zehnder interferometer and Sagnac loop, Phys. Scr., 94, 125502, 2019. *https://doi.org/10.1088/1402-4896/ab3375*

[14] Y. Chang, L. Pei, T. Ning, J. Zheng, J. Li, C. Xie, Switchable and tunable multi-wavelength fiber ring laser employing a cascaded fiber filter, Opt. Fiber Technol., 58, 102240, 2020. *https://doi.org/10.1016/j.yofte.2020.102240*

[15] L. Zhang, Z. Tian, N.-K. Chen, H. Han, C.-N. Liu, K.T.V. Grattan, B.M.A. Rahman, H. Zhou, S.-K. Liaw, C. Bai, Room-temperature power-stabilized narrow-linewidth tunable erbium-doped fiber ring laser based on cascaded Mach-Zehnder interferometers with different free spectral range for strain sensing, J. Light. Technol., 38, pp. 1966–1974, 2020. *https://doi.org/10.1109/JLT.2020.2971666*

[16] L. Xin, X. Zhou, J. Chen, Low threshold multi-wavelength erbium-doped fiber ring laser with NOLM and Lyot filter, Opt. Fiber Technol., 68, 102800, 2022. *https://doi.org/10.1016/j.yofte.2021.102800*

[17] S. Marrujo-García, I. Hernández-Romano, D.A. May-Arrioja, V.P. Minkovich, M. Torres-Cisneros, In-line Mach–Zehnder interferometers based on a capillary hollow-core fiber using vernier effect for a highly sensitive temperature sensor, Sensors., 21, 5471, 2021. *https://doi.org/10.3390/s21165471*

[18] S. Marrujo-García, L.A. Herrera-Piad, I. Hernández-Romano, D.A. May-Arrioja, V.P. Minkovich, M. Torres-Cisneros, Narrow spectral linewidth and tunable erbium-doped fiber ring laser using a MZI based on CHCF, Opt. Fiber Technol., 67, 102739, 2021. *https://doi.org/10.1016/j.yofte.2021.102739*

ISSN 2524-2121

HERRERA-PIAD, Luis, VELAZQUEZ-GONZALEZ, Felipe, DURAN-PEREZ, Oscar and BRIANZA-GORDILLO, Gerardo. Switchable emissions of an Erbium-doped fiber laser using cascaded MZIs based on CHCF. ECORFAN Journal-Taiwan. 2023

Article **ECORFAN Journal- Taiwan**
June, 2023 Vol.7 No.13 7-15

Identification of an instrumental proposal based on fiber optic sensors of the Bragg grating type for implementation in an experimental platform for dynamic analysis

Identificación de propuesta instrumental basada en sensores fibra óptica del tipo rejilla de Bragg para implementación en plataforma experimental de análisis dinámicos

HERNÁNDEZ-GONZÁLEZ, Josué Iván †, TORRES-CEDILLO, Sergio Guillermo*, HERNÁNDEZ-MORENO, Hilario and CORTÉS-PÉREZ, Jacinto

SEPI-ESIME Ticomán. Instituto Politécnico Nacional.
Centro Tecnológico Aragón, FES – Universidad Nacional Autónoma de México.

ID 1st Author: *Josué Iván, Hernández-González* / **ORC ID:** 0009-0003-5489-1611, **CVU CONAHCYT ID:** 1270905

ID 1st Co-author: *Sergio Guillermo, Torres-Cedillo* / **ORC ID:** 0000-0002-3297-6409, **CVU CONAHCYT ID:** 229481

ID 2nd Co-author: *Hilario, Hernández-Moreno* / **ORC ID:** 0000-0002-4055-0037, **CVU CONAHCYT ID:** 40443

ID 3rd Co-author: *Jacinto, Cortés-Pérez* / **CVU CONAHCYT ID:** 209116

DOI: 10.35429/EJT.2023.13.7.7.15 Received March 12, 2023; Accepted June 30, 2023

Abstract

Recently it has been reported the use of non-invasive methods for the identification and monitoring of vibrational parameters in rotodynamic systems, such as aircraft engines, which require the implementation of innovative detection systems, such as fiber optic sensors, which overcome deficiencies of adaptability to adverse environments such as intense magnetic fields and the impossibility of performing a distributed detection of vibrations, limitations present in the sensors conventionally based on capacitive or piezoelectric principles. Therefore, in the present study, through the use of an experimental platform for dynamic analysis, the best proposal of an instrumental system based on fiber optic sensors with Bragg gratings was selected for its use in vibrational measurement and analysis, through the theoretical study of the different approaches to vibrational analysis using fiber optic sensors with Bragg gratings. The analysis of the results of the study presents a justification of the type of instrumental proposal selected from the characteristics provided by the experimental platform. In addition, the experimental proposal will be implemented in the future and may contribute to the development of other vibrational studies.

Fiber Bragg Grating (FBG), Vibration monitoring, Instrumental system

Resumen

Recientemente se ha reportado el empleo de métodos no invasivos para la identificación y monitoreo de parámetros vibracionales en sistemas rotodinámicos; tales como los motores de las aeronaves, los cuales requieren de la implementación de innovadores sistemas de detección; como son los sensores de fibra óptica, los cuales subsanan deficiencias de adaptabilidad a entornos adversos como son los campos magnéticos intensos y la imposibilidad de realizar una detección distribuida de las vibraciones, limitaciones presentes en los sensores basados convencionalmente en principios capacitivos o piezoeléctricos. Por lo que, en el presente estudio a través del empleo de una plataforma experimental para análisis dinámicos, se seleccionó la mejor propuesta de sistema instrumental basado en sensores fibra óptica con rejillas de Bragg; para su empleo en medición y análisis vibracional, a través del estudio teórico de los diferentes enfoques que abarcan los análisis vibracionales empleando sensores fibra óptica con rejilla de Bragg. El análisis de resultados del estudio presenta una justificación fundamentada del tipo de propuesta instrumental seleccionada a partir de las características que proporciona la plataforma experimental. Además, la propuesta experimental será implementada en un futuro y puede contribuir al desarrollo de otros estudios vibracionales.

Fibras con rejillas de Bragg (FBG), Monitoreo vibracional, Sistema instrumental

Citation: HERNÁNDEZ-GONZÁLEZ, Josué Iván, TORRES-CEDILLO, Sergio Guillermo, HERNÁNDEZ-MORENO, Hilario and CORTÉS-PÉREZ, Jacinto. Identification of an instrumental proposal based on fiber optic sensors of the Bragg grating type for implementation in an experimental platform for dynamic analysis. ECORFAN Journal-Taiwan. 2023. 7-13: 7-15

* Correspondence to Author (e-mail: storresc@ipn.mx)
† Researcher contributing as first author.

Introduction

Nowadays, dynamic analysis is highly relevant to ensure the safety and stability of modern engineering systems such as those encompassed in the area of mechanics and civil infrastructure; which require the use of non-destructive measuring instruments for real-time inspection of vibration signals that are important references for dynamic diagnosis, failure prevention and optimization design (Au *et al*., 2008; T. Li, Guo, *et al*., 2020; Xiong *et al*., 2021).

Particularly within the aviation and space industry, vibration not only interferes singularly with the monitoring of aircraft structural integrity, but can also affect other areas such as control and stability systems; and additionally it is not conducive to the physical and mental health of passengers and crew (Fan *et al*., 2011; Kong *et al*., 2022). According to Fan *et al*. (2011), it is of relevance to distinguish that flexible surfaces such as the wing have a high tendency to vibrate and these effects can be transmitted to the fuselage. In this sense, one of the main sources contributing to the presence of vibrations in the case of commercial aircraft, is the propulsion system; which is typically positioned at the bottom of the wing surface (Torres Cedillo *et al.*, 2019).

Recently, it has been reported the use of non-invasive techniques or methods for the identification of failures in rotodynamic systems; such as aircraft engines, where it is not possible to disassemble the rotating elements during their operation, consequently modern monitoring systems are required in order to avoid accidents or economic losses (Torres Cedillo *et al*., 2019).

Based on the above, an experimental platform of reduced size was designed and built, representative of the structure of a rotodynamic system with the capacity to reach an operating speed of up to 3600 RPM (see Figure 1), located at the facilities of the Centro Tecnológico de la Facultad de Estudios Superiores Aragón of the Universidad Nacional Autónoma de México.

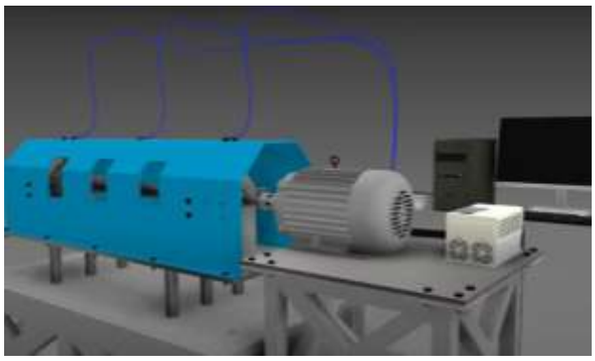

Figure 1 Experimental platform at scale of the structure of a rotodynamic system
Author's development

Currently, the experimental platform presented in Figure 1 is instrumented from the implementation of piezoelectric sensors of the accelerometer type. In this sense, within the experimental bases of dynamic analysis, the implementation of electrical sensors conventionally based on piezoelectric or capacitive principles is generally used, such is the case of accelerometers and strain gauges, respectively (T. Li, Guo, *et al*., 2020). Kong *et al*. (2022), state that the use of strain gauges for the measurement of deformations in the plane of the structure can be used for the estimation of structural vibration parameters such as displacements, rotation angles and angular velocities; which can be part of a complete detection of dynamic vibrations.

On the other hand, accelerometers are a key equipment in vibration measurement and the important role they play. However, both sensors use a weak voltage signal, which daily presents complications for their adaptation in hostile environments as a result of intense magnetic fields, the use of complex wiring joints and the impossibility of a distributed vibration detection, which will limit the long-term monitoring practices and therefore; it is required the implementation of innovative sensors with capabilities to adapt to this type of environment (T. Li, Guo, *et al*., 2020; Xiong *et al*., 2021).

The proposed solution to the problem explained above is the use of fiber optic sensor technology, especially of the Bragg grating type, which has generated interest in recent years in a wide range of applications, including the monitoring of mechanical properties such as strain, temperature, stress, vibration, pressure, force, displacement, directional curvature, among others (Xu *et al*., 2020).

ISSN 2524-2121

This is due to a number of numerous inherent advantages of which their compact size and light weight, passive sensing capability, operation in harsh environmental conditions, invulnerability to electromagnetic fields, high sensitivity and good corrosion resistance stand out (Chen *et al.*, 2018; Khalid *et al*., 2021; T. Li, Guo, *et al*., 2020).

Added to this, optical sensors based on the principle of operation by wavelength, such as Bragg gratings inscribed in optical fiber present the ability to be installed at multiple detection points using a single fiber, which allows them to be analyzed by multiplexing interrogation techniques by time, frequency or wavelength, which significantly reduces the cost of the measurement system since only one light source and a single detection system are needed, as exposed by Garcia *et al*. (2020). One of the important features specifically in wavelength interrogation is the ability to be unaffected by signal intensity because the strain information is provided, as the name implies, through the wavelength (Hernández-Moreno *et al*., 2009).

As a result of these advantages, fiber optic Bragg grating (FBG) based sensors are excellent solutions for a variety of structural integrity monitoring problems; being able to be inserted into concrete or composite materials, in addition to the ability to perform shape detection, vibration suppression control in complicated civil structures such as bridges or roads and other engineering fields, such as chemical testing and inspection and aggressive environments, including sensors for oil and gas wells and seismic instruments (Garcia et al., 2010; Goossens *et al*., 2021; Kong *et al*., 2022).

Method

This study seeks to identify the best solution for the construction of an experimental instrumental dynamic monitoring system (conditioned to the use of an optical detection interrogator model si425 from Micron Optics, see Figure 2) to replace the current monitoring system based on accelerometers; The objective is to obtain as a result a solid approach of a monitoring system that adapts to the available resources in terms of economy and available material for the vibrational study of the experimental platform.

Figure 2 Micron Optics optical detection interrogator model si425. *Luna / Micron Optics SI425-300 Optical Sensing Interrogator (n. f.)*

Theoretical framework

Fiber optic sensors can be broadly classified into two types of group, extrinsic and intrinsic; the sensors of the first group are distinguished in that the detection is performed in a region outside the fiber, on the other hand; the sensors of the second type present the detection inside the optical fiber itself (Garcia *et al*., 2010). However, fiber optic sensors can also be classified by the principle of operation as described by Garcia *et al*. (2010) in their research and presented below.

Sensors based on light intensity: This kind of sensors present as relevant characteristics a low acquisition cost, a large measurement bandwidth and the possibility of using both reflection and transmission modes (T. Li, Guo, *et al*., 2020). Generally speaking, they can be classified into two categories as mentioned by García *et al*. (2010), depending on whether or not they present physical contact with the vibrating object to be analyzed, in this sense the non-contact structures use a reflective signal to detect vibration, while the other structures use the transmissive configuration.

Fundamentally, the light intensity is modulated by a transducer device, guided to a detector and subsequently processed into electronic signals; to keep this type of sensor calibrated, it is necessary to have a reference mechanism that avoids errors due to optical power fluctuations in the system due to the source, couplers, connectors or any optical component that may introduce significant relative errors and it is also important to consider that they suffer from an unstable measurement caused by the uncertain curvature of the fiber (Di *et al.*, 2018).

ISSN 2524-2121

Interferometry-based sensors: This type of optical sensor better known as Fabry-Pérot interferometer, consists of a basic structure of two flat and parallel surfaces with partial reflectivity that create interference patterns as exposed by García *et al*. (2010). In the first type, partial mirror surfaces must be created inside the fiber by chemical or fusion processes; on the other hand, in the extrinsic version of the interferometer, the optical cavity is external to the fiber and is kept aligned by means of an attached capillary tube (García *et al*., 2010). Although well-structured arrays can be built using this type of sensors and present characteristics such as high coupling efficiency, stability, ease of alignment, good resolution, accuracy and become considered the most popular technique for vibration detection in the area of fiber optics, it suffers from a limitation of bandwidth and a complicated measurement system at a high price (T. Li, Guo, *et al*., 2020).

Wavelength-based sensors: Fiber optic Bragg grating sensors have been used since 1988 to measure deformations and temperatures, from the multiple advantages they present such as those mentioned above, which have led to a significant increase in the amount of developed works where FBGs are implemented to measure vibrations (Garcia *et al*., 2010).

Vibrations induce high-speed dynamic deformation variations and monitoring the position of the FBG resonance wavelength allows measuring those vibrations, despite the fact that to detect high-frequency vibrations, high-speed interrogation techniques are needed. These fiber optic sensors offer accurate, durable and inexpensive configurations for measuring vibrations, which expands the range of applications, opens new fields of research and makes them excellent candidates for measuring vibrations; therefore they are the type of sensor to be employed in the development of this study and further study of these is discussed below (T. Li, Pan, *et al*., 2020).

Approach to vibration studies using FBG

Within the multiplicity of applications of FBG sensors, through the study of previous research for the development of this research, it was possible to identify two approaches directly related to the branch of mechanics and civil infrastructure.

The first one deals with the development of optical sensors of the accelerometer type using FBG and the second one about experimental arrays built for the monitoring of engineering systems.

The first of these approaches, is related according to the vibration-strain coupling difference of FBG, these vibration sensors can be classified into three categories, which are mentioned by Li, Guo *et al*. (2020) and described as follows.

1) Vibration sensors based on bonded FBG: These sensors are responsible for converting the vibration signal into the surface tension of the elastomer (usually a beam in cantilever configuration) detected by the bonded FBG as shown in Figure 3, this configuration is the most widely used due to its simple principle and structure (T. Li, Guo, *et al*., 2020).

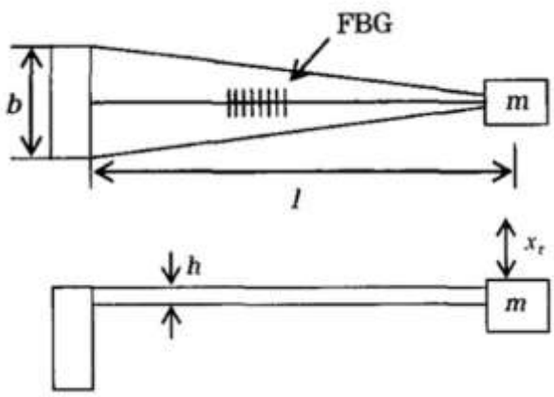

Figure 3 Sensors based on glued FBG
T. Li, Guo, et al., 2020

2) FBG axial property based vibration sensors: The axial property of the FBG based vibration sensor is adjusted by suspending the FBG in the sensor configuration instead of a bonded FBG as shown in Figure 4 (Basumallick *et al*., 2020). Going into detail, these configurations are more complex since a mass is incorporated in the center of such a fiber with both ends attached to the base of the sensor and elastomer, respectively; where vibration along the length of the fiber must be converted into compression or tension of the FBG (T. Li *et al*., 2017).

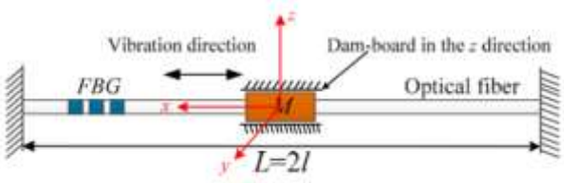

Figure 4 Sensors based on the axial property
T. Li, Guo, et al., 2020

3) Vibration sensors based on the transverse property of FBG: Similarly, both ends of a FBG are fixed to design the transverse property of vibration sensors as presented in Figure 5; despite this, the inertial force of the vibrating mass is exerted in the transverse direction instead of the direction along the fiber length (K. Li *et al*., 2014). These configurations can amplify the compression or tension of the FBG, leading to higher sensitivity for a transverse force compared to the axial force along the fiber (K. Li *et al*., 2014; T. Li, Guo, *et al*., 2020).

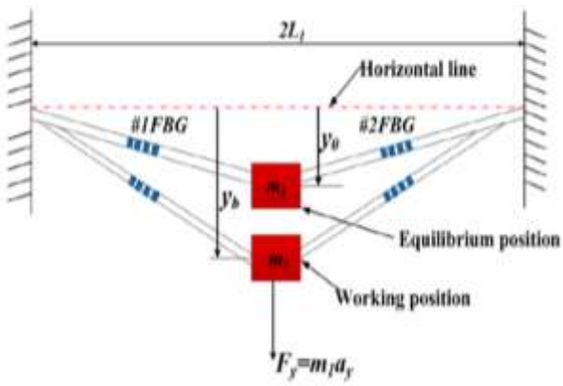

Figure 5 Sensors based on the transverse property
T. Li, Guo, et al., 2020

Until these days, a considerable number of optical accelerometer designs employing FBG have been developed, which aims to achieve a high frequency measurement response range and the development of techniques to considerably increase the sensitivity, which make this approach as a potential option for monitoring the vibrational responses of the experimental platform.

The second approach to the construction of experimental arrays for the monitoring of vibrating systems, basically consists of placing an FBG sensor on the structure to be analyzed; this is because any change in deformation, temperature and vibration is transmitted directly on the grid in terms of wavelength shift, as argued by Goossens *et al*. (2021). The way of placing the FBGs can be in the form of minimal intrusion in the case of insertion or mounted on the surface to be analyzed. Davis *et al*. (1996) state that it is important to be aware that one of the challenges is the location of the sensors throughout the structure, and one must be meticulous with the method of attachment or insertion of the sensors as it may present problems in the long term due to the effects present in the material.

From the above, there are details regarding how fibers are inserted into the material, while benefiting from intrinsic protection from the host material conditions, not all manufacturing methods in the case of composite materials allow for fiber insertion, in addition; it can be challenging to ensure the optical connection reliability of the sensor and in case of failure it is difficult to repair the fibers; these limitations can restrict the implementation of fibers in many composite applications (Goossens *et al*., 2021).

The amount of research related to this type of approach is very reduced; this is a consequence of the need for interrogation systems with peculiar characteristics, which will be discussed below. In this sense, some of the works of relevance are that of Rajan and Karekal (2017), which deals with a study of rock cracking events for mining applications adjunctly employing an FBG sensor for acoustic emission monitoring, using a high frequency FBG interrogation system with sampling capacity of 1.16 MHz.

Another work is presented by Kim *et al*. (2022), which deals with an experimental study in which several FBG networks are used to detect vibro-acoustic signals from leaking water pipes using an interrogation system with 3 kHz sampling capability. Similarly, Tozzetti *et al*. (2021), showed an experimental study about dynamic deformation measurements in gasoline direct injectors where FBGs were placed on the surface of a valve body along the axial direction, this employing an interrogation system with measurement capability up to 240 MHz.

ISSN 2524-2121

And finally Jang and Kim (2017), developed a study of low-velocity impact-induced delamination in carbon fiber reinforced polymer laminates where several FBGs were bonded to the laminate surface and implementing a high-speed interrogation system with a relatively low sampling frequency of 100 kHz.

Given the simple and multitasking characteristics of the implementation of this type of approach, despite the limitations described above, it is undoubtedly a good option for monitoring the vibrational analysis of the experimental platform.

Monitoring systems using fiber optics with Bragg gratings

Going deeper into the two previous approaches described above, the use of two types of instruments for the optical monitoring system was identified, the first one through the use of modulators and the second one using interrogators. Since part of the objective of the study is conditioned to the use of the si425 optical interrogator, the review of these monitoring systems was limited to this type of optical instruments.

In most of the researches, sophisticated vibration detection systems are developed for vibration monitoring in a high frequency measurement range, allowing the use of a wide range of electro-optical components adjusting to the required needs and available economic resources, such as the monitoring systems developed and described below.

One of the most outstanding developments is that of Kim *et al*. (2022), where they conceived a spectrometer-type interrogation system where the reflected wavelengths feed a photodiode array module through a fiber optic circulator to demodulate the Bragg wavelength. Buck *et al*. (2012), on the other hand, designed a highly integrated interrogator based on an ordered waveguide grating, specially constructed for the acquisition of dynamic structural loads. Xiong *et al*. (2021), generated an eight-channel FBG wavelength interrogator to achieve real-time wavelength recording outputs under the spectroscope-type operating principle with an acquisition frequency of 10 Hz.

On the other hand; Yamaguchi and Shinoda (2015), established a fast wavelength-scanning laser interrogator capable of measuring vibrations with sampling frequency of 20 MHz. And by Isago and Nakamura (2009), they contributed a FBG sensor array system employing a high-speed 172 kHz high-speed scanning light source.

However, there are also works where commercial interrogators are used such is the case of Fan *et al*. (2011), where they performed surface testing and identification of vibration parameters using a Micron Optics si425 interrogator, which works as a scanning laser system, capable of an acquisition frequency of 250 Hz. One of the widely used interrogators is the SM130 from Micron Optics which operates as a scanning laser system and is used by Basumallick *et al*. (2020) and Xu *et al*. (2020), respectively; for recording the response of FBG accelerometers with a scan rate of 2 kHz and in acceleration tests from 1 to 100 Hz. Another type of commercial interrogators with outstanding characteristics are those employed in research such as Zhang *et al*. (2007), where they used a high-speed CGT (Circulating Grating Transform) interrogator developed by ITF Labs which reaches a sampling rate of up to 5 kHz and the Thor-LABS alternative interrogation system with 1 kHz interrogation capability operating under the spectroscopy operating principle employed by Macedo *et al*. (2023).

Proposed vibrational monitoring system

To determine the best solution to our identified problem, it is known that; the experimental platform reaches an angular velocity of 3600 RPM, equivalent to a frequency of 60 Hz, from this, it is proposed that the experimental instrumental system to be developed for the dynamic monitoring of the experimental platform, using an optical detection interrogator model si425 of the manufacturer Micron Optics; is the construction of the experimental arrangement using FBG sensors which are attached to the surface of the platform, as shown in Figure 6, so that any change in terms of vibration is transmitted directly on the grid as a function of the wavelength shift.

ISSN 2524-2121

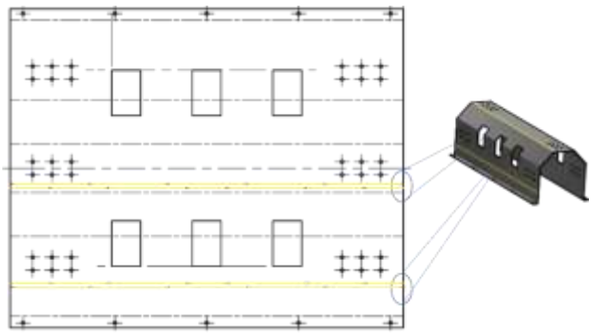

Figure 6 Experimental setup using FBG adhered to the platform surface
Author's development

Results

It was decided to choose to develop an experimental system where FBG sensors are attached to the platform because in this way through the multiplexing properties of the FBG more points can be obtained to analyze on the platform, in addition; although the development of optical accelerometers using FBG sensors presents a potential growth from the high sampling rates that can reach in the measurement range of up to MHz, for this application these high levels of vibrational analysis are not required; Therefore, the detection capabilities provided by these accelerometers would not be taken advantage of, added to this, the design of a FBG accelerometer requires great investment in economic terms, time and effort, which would delay the start of the experimental tests.

On the other hand, although to measure vibrations using FBG sensors, an interrogation system with a sufficiently high bandwidth is needed as described by García *et al*. (2010); in accordance with what is stated by Preizler *et al*. (2017), where they mention that the Nyquist theorem requires the sampling rate to be at least twice the bandwidth, assuming that the actual sampling takes an infinitely short time; in this sense by presenting the experimental platform with a sampling frequency 60 Hz, a bandwidth of 120 Hz is required in order to be able to perform the vibration measurement acquisition effectively, therefore; Although the si425 interrogator has a bandwidth of 250 Hz, which compared to the interrogation systems built in the research reviewed is very low, it has the capacity to be used in this experimental arrangement.

Conclusions

In this study, the review of two of the main approaches in the experimental dynamic analysis of engineering systems using fiber optic sensors of the Bragg grating type was carried out, with the objective of identifying the best solution for the vibrational analysis of the experimental platform presented and the use of the si425 optical interrogator, the proposal of an experimental arrangement was selected, which fits perfectly to the characteristics of the vibrational analysis to be carried out in the future, which can contribute in an extrapolated way to more detailed dynamic studies such as modal analysis and the estimation of aircraft propulsion systems balancing, which would benefit the maintenance procedures in the industry in such a way that the structural health of the aircraft and the physical and mental integrity of the passengers are taken care of. In addition to this, the presented review can contribute to the decision making process of other studies where the selection of an instrumental proposal for vibrational analysis is required.

Acknowledgments

This research was carried out thanks to the UNAM-PAPIIT Program through projects IN113921 and IN110923. Additionally, we are grateful to the IPN-SIP project 20231219 for the support to present the results obtained in this congress and to CONAHCYT for their support through the national scholarship program and the researcher system (SNI).

References

Au, H. Y., Khijwania, S. K., & Tam, H. Y. (2008). Fiber Bragg grating based accelerometer (D. D. Sampson, Ed.; p. 70042S). https://doi.org/10.1117/12.785992

Basumallick, N., Bhattacharya, S., Dey, T. K., Biswas, P., & Bandyopadhyay, S. (2020). Wideband Fiber Bragg Grating Accelerometer Suitable for Health Monitoring of Electrical Machines. IEEE Sensors Journal, 20(24), 14865–14872. https://doi.org/10.1109/JSEN.2020.3011414

Buck, T. C., Müller, M. S., & Koch, A. W. (2012). Fiber Bragg grating (FBG) sensor systems for monitoring of dynamic structural loads. International Multi-Conference on Systems, Signals and Devices, SSD 2012 - Summary Proceedings. https://doi.org/10.1109/SSD.2012.6198067

Chen, T., Ye, M. li, Liu, S. liang, & Deng, Y. (2018). Experimental study on cross-sensitivity of temperature and vibration of embedded fiber Bragg grating sensors. Optoelectronics Letters, 14(2), 92–97. https://doi.org/10.1007/s11801-018-7228-5

Davis, M. A., Kersey, A. D., Sirkis, J., & Friebele, E. J. (1996). Shape and vibration mode sensing using a fiber optic Bragg grating array. Smart Materials and Structures, 5(6), 759–765. https://doi.org/10.1088/0964-1726/5/6/005

Di, H., Xin, Y., & Jian, J. (2018). Review of optical fiber sensors for deformation measurement. Optik, 168, 703–713. https://doi.org/10.1016/j.ijleo.2018.04.131

Fan, H., Yi, X., & He, J. (2011). Surface testing and parameter identification of vibration. Proceedings - 3rd International Conference on Measuring Technology and Mechatronics Automation, ICMTMA 2011, 3, 617–620. https://doi.org/10.1109/ICMTMA.2011.725

García, Y. R., Corres, J. M., & Goicoechea, J. (2010). Vibration detection using optical fiber sensors. In Journal of Sensors (Vol. 2010). https://doi.org/10.1155/2010/936487

Goossens, S., Berghmans, F., Muñoz, K., Jiménez, M., Karachalios, E., Saenz-Castillo, D., & Geernaert, T. (2021). A global assessment of barely visible impact damage for CFRP sub-components with FBG-based sensors. Composite Structures, 272. https://doi.org/10.1016/j.compstruct.2021.114025

Hernández-Moreno, H., Collombet, F., Douchin, B., Choqueuse, D., Davies, P., & González Velázquez, J. L. (2009). Entire Life Time Monitoring of Filament Wound Composite Cylinders Using Bragg Grating Sensors: II. Process Monitoring. Applied Composite Materials, 16(4), 197–209. https://doi.org/10.1007/s10443-009-9088-4

Isago, R., & Nakamura, K. (2009). A high reading rate fiber Bragg grating sensor system using a high-speed swept light source based on fiber vibrations. Measurement Science and Technology, 20(3). https://doi.org/10.1088/0957-0233/20/3/034021

Jang, B. W., & Kim, C. G. (2017). Real-time detection of low-velocity impact-induced delamination onset in composite laminates for efficient management of structural health. Composites Part B: Engineering, 123, 124–135. https://doi.org/10.1016/j.compositesb.2017.05.019

Khalid, N. S., Hassan, M. F., Zohari, M. H., & Rahim, M. R. (2021). A strain-wavelength modelling of low-frequency cantilever fibre Bragg grating accelerometer. Proceedings of the Institution of Mechanical Engineers, Part C: Journal of Mechanical Engineering Science, 235(23), 6711–6723. https://doi.org/10.1177/09544062211008929

Kim, D. G., Lee, A., Park, S. W., Yeo, C., Bae, C., & Park, H. J. (2022). Experimental Study on Leak-induced Vibration in Water Pipelines Using Fiber Bragg Grating Sensors. Current Optics and Photonics, 6(2), 137–142. https://doi.org/10.3807/COPP.2022.6.2.137

Kong, C., Zhao, D., Zhang, J., & Liang, B. (2022). Real-Time Virtual Sensing for Dynamic Vibration of Flexible Structure via Fiber Bragg Grating Sensors. IEEE Sensors Journal, 22(22), 21706–21718. https://doi.org/10.1109/JSEN.2022.3212070

Li, K., Chan, T. H. T., Yau, M. H., Thambiratnam, D. P., & Tam, H. Y. (2014). Experimental verification of the modified spring-mass theory of fiber Bragg grating accelerometers using transverse forces. Applied Optics, 53(6), 1200. https://doi.org/10.1364/AO.53.001200

Li, T., Guo, J., Tan, Y., & Zhou, Z. (2020). Recent Advances and Tendency in Fiber Bragg Grating-Based Vibration Sensor: A Review. IEEE Sensors Journal, 20(20), 12074–12087. https://doi.org/10.1109/JSEN.2020.3000257

ISSN 2524-2121

Li, T., Pan, A., & Ren, H. (2020). A High-Resolution Triaxial Catheter Tip Force Sensor With Miniature Flexure and Suspended Optical Fibers. IEEE Transactions on Industrial Electronics, 67(6), 5101–5111. https://doi.org/10.1109/TIE.2019.2926052

Li, T., Tan, Y., Han, X., Zheng, K., & Zhou, Z. (2017). Diaphragm Based Fiber Bragg Grating Acceleration Sensor with Temperature Compensation. Sensors, 17(12), 218. https://doi.org/10.3390/s17010218

Luna / Micron Optics SI425-300 Optical Sensing Interrogator. (s. f.). Artisan Technology Group. https://www.artisantg.com/TestMeasurement/56146-1/Micron-Optics-si425-Optical-Sensing-Interrogator

Macedo, L., Pedruzzi, E., Avellar, L., Castellani, C. E. S., Segatto, M. E. V., Frizera, A., Marques, C., & Leal-Junior, A. (2023). High-Resolution Sensors for Mass Deposition and Low-Frequency Vibration Based on Phase-Shifted Bragg Gratings. IEEE Sensors Journal, 23(3), 2228–2235. https://doi.org/10.1109/JSEN.2022.3231434

Preizler, R. R., Davidi, R., Motil, A., Botsev, Y., Hahami, M., & Tur, M. (2017). On the actual bandwidth of some dynamic fiber optic strain/temperature interrogators. 25th International Conference on Optical Fiber Sensors, 10323, 103235C. https://doi.org/10.1117/12.2267504

Rajan, G., & Karekal, S. (2017). High Frequency Fibre Bragg Grating Interrogator for Monitoring Rock Cracking Events for Mining Applications. Proceedings - 2017 2nd International Conference of Fibre-Optic and Photonic Sensors for Industrial and Safety Applications, OFSIS 2017, 45–51. https://doi.org/10.1109/OFSIS.2017.12

Torres Cedillo, S. G., Al-Ghazal, G. G., Bonello, P., & Cortés Pérez, J. (2019). Improved non-invasive inverse problem method for the balancing of nonlinear squeeze-film damped rotordynamic systems. Mechanical Systems and Signal Processing, 117, 569–593. https://doi.org/10.1016/j.ymssp.2018.07.032

Tozzetti, L., Barsanti, T., Gambini, F., Manzo, G., Filippi, S., Matteucci, L., Izzo, I., Di Pasquale, F., & Faralli, S. (2021). Fiber Bragg Grating Sensors for Dynamic Strain Measurements in Gasoline Direct Injectors. IEEE Transactions on Vehicular Technology, 70(6), 5658–5668. https://doi.org/10.1109/TVT.2021.3081363

Xiong, L., Guo, Y., Zhou, W., Chen, M., & Zhou, X. (2021). Fiber Bragg Grating-Based Three-Axis Vibration Sensor. IEEE Sensors Journal, 21(22), 25749–25757. https://doi.org/10.1109/JSEN.2021.3118360

Xu, H., Li, F., Gao, Y., & Wang, W. (2020). Simultaneous Measurement of Tilt and Acceleration Based on FBG Sensor. IEEE Sensors Journal, 20(24), 14857–14864. https://doi.org/10.1109/JSEN.2020.3010851

Yamaguchi, T., & Shinoda, Y. (2015). Development of fast FBG interrogator with wavelength-swept laser. Optical Sensors 2015, 9506, 95061F. https://doi.org/10.1117/12.2177881

Zhang, X., Max, J.-J., Jiang, X., Yu, L., & Kassi, H. (2007). Experimental investigation on optical spectral deformation of embedded FBG sensors. Photonics Packaging, Integration, and Interconnects VII, 6478, 647808. https://doi.org/10.1117/12.700807

ISSN 2524-2121

Article **ECORFAN Journal- Taiwan**
June, 2023 Vol.7 No.13 16-31

Comparative study of the effects caused by polymers, bubbles and surfactants in a turbulent flow

Estudio comparativo de los efectos causados por polímeros, burbujas y tensioactivos en un flujo turbulento

LÓPEZ AGUADO-MONTES, José Luis†, RIVERA-LÓPEZ, Jesús Eduardo, ARCINIEGA-MARTÍNEZ, José Luis and JUAREZ-NAVARRO, Carlos Alfonso

Instituto Politécnico Nacional, Escuela Superior de Ingeniería Mecánica y Eléctrica Unidad Azcapotzalco

ID 1st Author: *José Luis, López Aguado-Montes* / **ORC ID**: 0009-0009-6322-4937, **CVU CONAHCYT ID**: 229257

ID 1st Co-author: *Jesús Eduardo, Rivera-López* / **ORC ID**: 0000-0003-3988-9305, **CVU CONAHCYT ID**: 161653

ID 2nd Co-author: *José Luis, Arciniega-Martínez* / **ORC ID**: 0000-0003-4996-8146, **CVU CONAHCYT ID**: 161637

ID 3rd Co-author: *Carlos Alfonso, Juarez-Navarro* / **ORC ID**: 0000-0002-2466-7796

DOI: 10.35429/EJT.2023.13.7.16.31 Received March 22, 2023; Accepted June 30, 2023

Abstract

In the present work, the particle image velocimetry (PIV) technique was used to measure the velocity components in the direction normal and tangent to the wall to obtain average velocity fields, wall shear stresses, friction velocity, drag reduction and average deformation fields were obtained by adding bubbles (injected by electrolysis), polymer (WSR-301 polyox) and surfactant (cationic) and their bubble-polymer, bubble-surfactant and polymer-surfactant combinations at concentrations of 164 and 272 ppm in a water flow in a channel (2cm x 10cm x 160cm) with a Reynolds number of 5200. Increased levels of drag reduction were obtained when combining the techniques, for example in the bubbles with polymers (WSR - 301 polyox) combinations, drag reduction results of 82 and 93 % were obtained for the concentrations of 164 and 272 ppm respectively, While when the combinations of bubbles with surfactants were used, the results were 37 % for 164 ppm and only 16 % for 272 ppm, and for the combination of polymer with surfactant for 164 ppm the results were 47 % and for 272 ppm the drag increased by 25 %, possibly due to an incorrect preparation of the polymer or surfactant, which leads to the conclusion that the greatest synergistic benefit is presented when combining the drag reducing techniques of bubbles and polymers.

Bubbles, Polymers, Surfactant

Resumen

En el presente trabajo se usó la técnica de velocimetría de imagen de partículas (PIV) para medir las componentes de velocidad en dirección normal y tangente a la pared con lo que se obtuvieron campos de velocidad promedio, esfuerzos de corte en la pared, velocidad de fricción, reducción del arrastre y campos de deformación promedio adicionando burbujas (inyectadas por electrolisis), polímero (polyox WSR-301) y surfactante (catiónico) y sus combinaciones burbujas-polímeros, burbujas-surfactanes y polimeros-surfactantes en concentraciones de 164 y 272 ppm en un flujo de agua en un canal (2cm x 10cm x 160cm) con un número de Reynolds de 5200. Se obtuvieron incrementos en los niveles de reducción del arrastre al combinar las técnicas, por ejemplo en las combinaciones burbujas con polímeros (polyox WSR - 301) se tuvieron resultados en la reducción del arrastre del 82 y 93 % para la concentraciones de 164 y 272 ppm respectivamente, mientras que cuando se utilizaron las combinaciones de burbujas con surfactantes se tuvo 37 % para 164 ppm y apenas 16 % para 272 ppm y para la combinación polímero con surfactante para 164 ppm se tuvo 47 % y para 272 ppm el arrastre aumentó en 25 % posiblemente debido a una incorrecta preparación del polímero o del surfactante, por lo que se llega a la conclusión de que el mayor beneficio sinérgico se presenta al combinar las técnicas reductores del arrastre de burbujas y polímeros.

Burbujas, Polímeros, Surfactanes

Citation: LÓPEZ AGUADO-MONTES, José Luis, RIVERA-LÓPEZ, Jesús Eduardo, ARCINIEGA-MARTÍNEZ, José Luis and JUAREZ-NAVARRO, Carlos Alfonso. Comparative study of the effects caused by polymers, bubbles and surfactants in a turbulent flow. ECORFAN Journal-Taiwan. 2023. 7-13: 16-31

† Researcher contributing as first author.

Introduction

The production and the way in which energy is used generate an environmental impact at all scales, threatening future development. The abundance of energy as well as the lack of awareness about the impact of its use on the environment have facilitated, on the one hand, human, commercial and industrial activities of intensive and inefficient energy consumption and, on the other hand, the disorderly growth of cities, which today are real machines of energy consumption as well as producing huge amounts of waste that are devouring the natural environment.

Therefore a large number of systems are designed to transport a fluid from one place to another with a specified expense, speed and elevation difference, during this process the system can generate mechanical work in a turbine or it can consume this type of work in a pump or a fan (M. A. Asidin, E. Suali, T. Josnukin, F. A. Lahin, 2019).

For these reasons the phenomenon of drag reduction in pipelines has received much attention for decades due to its potential applications in engineering, especially in the fluid transport industry. Various methods to improve drag reduction have been developing over the past few years and are divided into 2 categories mainly; additive methods and non-additive methods. Drag reduction using a polymer as an additive is one of the most attractive and studied methods. Reducing drag in pipelines means using less pump power to move a fluid thus offering economic savings for companies (White F. , 2008). Recent research on improving heat transfer in pipe flow shows that thermal performance is generally accompanied by an increase in pressure drop.

To solve this problem the development of drag reduction technology is very promising and researches on this topic have attracted more and more attention (Weichi Gang, Jun Shen, Wei Dai, Ke Li, Maoqiong Gang, 2021). That is why the implementation of drag reduction technologies to the various means of transport or pumping systems, represent savings of billions of dollars annually, and thus, being that the issue of turbulent drag reduction is not new, it has resumed a new worldwide boom due to the large amount of money that could be saved.

Drag reduction was defined as a reduction in the pressure drop of a turbulent flow in a pipe due to the addition of a drag reducer (bubbles, polymers, surfactants, etc.) as they cause a reduction of the shear stress in the wall τ_{wall} or the coefficient of friction.

One definition of drag reduction is:

"Drag reduction is the decrease in the coefficient of friction of the mixture of the drag reductant with the solvent (substance that allows the dispersion of another substance in this at the molecular or ionic level) in a turbulent flow below the coefficient of the solvent (water for this experiment)" (Lumley, 1969).

This implies that the flow of the solution has to be turbulent, and that the coefficient of friction is less than that of Newtonian flow, provided that the mixture and the solvent are considered to have the same viscosity.

On the other hand, it has been seen that drag-reducing solutions are generally non-Newtonian, so that the viscosity of the drag-reducing solutions is less than that of Newtonian flow. Newtonian so that the viscosity is no longer a constant and this can be one of the main problems in describing the drag reduction phenomenon. Around this definition it is important to define the ratio of the friction factor or the shear stress ratio (τ_{wall}), for the solution with the subscript S and the Newtonian solvent with the subscript N:

$$C_\tau = \frac{\tau_{\text{wall}S}}{\tau_{\text{wall}N}} \tag{1}$$

The shear stress in the wall and the coefficient of friction are related by:

$$f = \frac{\tau_{\text{wall}}}{\frac{\rho}{2}\bar{\text{u}}^2} \tag{2}$$

Where $\bar{u}$ is the average velocity given by.

$$\bar{\text{u}} = \frac{Q}{A} \tag{3}$$

With Q being the flow rate and A being the cross-sectional area of the pipe. Therefore, it can also be written as:

$$Cf = \frac{f_S}{f_N} \tag{4}$$

ISSN 2524-2121

The most common, however, for reporting drag reduction is by percentage.

$$DR = 1 - \frac{f_s}{f_N} \quad o \; 1 - \frac{\Delta P_S}{\Delta P_N} \tag{5}$$

The phenomenon of drag reduction was first observed in 1948, where a reduction of over 50% was achieved with only 250 ppm of polymethyl methacrylate solution, which caused the interest of many researchers in the addition of polymers and surfactants in pipes and channels (Toms, 1948).

The addition of polymers to a turbulent flow causes a dramatic reduction in Reynolds stresses (Re) and in fluctuating velocities perpendicular to the flow direction (v'). Numerous works on drag reduction by adding polymers have been carried out in recent decades; a brief review of investigations on drag reduction by adding external agents follows.

The changes in turbulent structures are very important that is why a number of important parameters such as molecular weight, flexibility, length and expansion are mentioned, because the polymer molecules during the drag reduction phenomenon are stretched in the turbulent boundary layer resulting in an increase in the viscosity of the fluid (A.Gyr, H.W. Bewersdorff, 1995).

A study conducted in 2010 where a small amount of CTAC NaSal (75 ppm) was added and studied by pressure drop using a particle image velocimetry system where a drag reduction of 75% was achieved. As conclusions it was observed, firstly, that the pressure drop depends on the fluid velocity, secondly, the results obtained in the PIV show that the amount of concentrated surfactant solution is strongly affected. While in a fully turbulent flow the kinetic energy of the solution is small and the Reynolds stress negligible (Ferhat Hadri, Sylvain Guillou, 2010).

Although the drag reduction increases with increasing polymer concentration, an asymptote is reached where the addition of polymer is no longer beneficial. With the right choice of parameters, polymers can reduce drag beyond the limiting asymptote, eliminating turbulence and giving way to laminar flow. At large concentrations the laminar state becomes unstable, resulting in fluctuations.

The results indicate that the asymptotic state is directly disconnected from the obtained turbulence (George H. Choueiri, José M López, Björn Hof, 2018).

Another experimentation performed in 2018 used a solution of a cationic surfactant, Cetyl Methyl Ammonium Chloride and a nonionic polymer. Six different solutions with different concentrations were made at different temperatures from 25°C to 50°C. It was found that the mixed solution curves could be divided into; Enhanced Drag Reduction Zones, Stable Drag Reduction Zones and Destroyed Drag Reduction Zone. The addition of polymers also increased the drag reduction efficiency in the destroyed zone by providing a wider Reynolds number range. In addition, the results indicated that temperatures influenced more than concentrations, so raising the temperature to change the solution structure is more effective than increasing the amount of structures (Dongjie Liuun, Qinghui Wang unJinjia Wei, 2018).

An important problem of drag reduction in turbulent flow with polymers is the diameter effect. A new method was developed in which the Reynolds number along with the friction factor is transformed into the Prandtl-Von Karman number.

Where these new parameters are correlated in straight lines.

It was found that the slope and intersection of these straight lines can be predicted by empirical correlations involving diameter and polymer concentrations. Thus if *Re* and *f* of the flow of a small diameter pipe are known, these two correlations can predict the characteristics for large pipe diameters.

With this method most of the relative errors between predicted data and experimental data are within 20%, much better than the traditional scale (Xin Zhan, Xiaodong Dai, Jishi Zhao, Dengwei Jing, Fei Liu, Lei Li, Yanping Xin, Kun Liu., 2021).

Another research conducted in 2021 experimentally compared in a turbulent flow with three different additives; a flexible polymer, a rigid polymer and a surfactant.

ISSN 2524-2121

A high drag reduction of approximately 58% was achieved using the flexible polymer and a maximum drag reduction of 70% was achieved with the flexible polymer and surfactant. The flexible polymer and surfactant solution had a small shear viscosity, on the other hand, the rigid polymer solution had a large shear viscosity with considerable shear thinning. In addition the flexible polymer solution was the only one that exhibited a large extensional relaxation time during the experiment (Lucas Warwaruk, Sina Ghaemi, 2021).

While, in 2022, the feasibility of applying a cationic surfactant as a reducing agent was sought through rheological test and simulations. The results of the experiment showed that the surfactant, Cetyl Methyl Ammonium Chloride, has excellent thixotropy and the viscosity recovery rate for 300 seconds can reach 97%. In addition, the CTAC/NaSal (Sodium Silicate) solution has a high oil resistance and salt tolerance. If the oil concentration increases from 0 to 6000 ppm the viscosity only decreases by 8.24% if the salt concentration increases from 0 to 6000 ppm the maximum viscosity reached will be 87.08%. It should be noted that the CTAC/NaSal solution has good temperature resistance (Ying Yuan; Jiaqiang Jing; Ran Yin; Peiyu Jing; Jianfei Hu, 2022).

A study conducted with Al_2O_3 nanoparticles with concetrations of 100 ppm, 200 ppm and 300 ppm with a mixing duration of 30, 60 and 120 min respectively, with a circular pipe used as a comparison of a spiral pipe, the two pipes mounted horizontally. The results yielded that with Reynolds number between 4,000 and 20,000 show a high drag reduction of 38% in the spiral pipe (Yanuar, Sealtial Mau, Kurniawan T. Waskito, Okky A. Putra,Rifqi Hanif, 2017).

In a more recent study it was found that the addition of SiO_2 nanoparticles to the cationic polyamide(PAM) solution quite efficient in reducing drag, but only at higher flow velocities with Reynolds number above 6000. While at lower Reynolds no improvement is perceived. The addition of SiO_2 to the PAM solution plays a dual role. The first is an increase in flow resistance caused by Brownian motion of the particles, the second is a decrease in flow resistance caused by acting as nodes to protect the polymer chain from induced stress.

At an optimal concentration of nanoparticles and high Reynolds numbers, the latter effect is dominant, resulting in higher drag reduction performance (Xiaoping Li, Jiaxin Pan 1Jinwen Shi, Yanlin Chai, Songwei Hu, Qiaorong Han, Yanming Zhang, Xianwen Li, Dengwei Jing, 2023).

After having made a literature review over the last 70 years of both experimental and numerical studies that have been carried out on drag reduction by adding bubbles, polymers, surfactants independently and their combinations, it can be concluded that there are many investigations of drag reduction by adding bubbles by different methods, adding polymers either by injection or by creating a homogeneous solution with the solvent and adding surfactants.

However there are very few studies combining two of the above techniques, for that reason it was decided to carry out this study, where a turbulent flow of water in a channel (2 cm wide x 10 cm high x 160 cm long) was analyzed experimentally, adding first bubbles, polymers and surfactants for the concentrations of 164 and 272 ppm independently and then adding the combinations of bubbles with polymers, bubbles with surfactants and polymers with surfactants also for the concentrations of 164 and 272 ppm, The drag reduction obtained by combining two techniques was greater than that obtained with a single technique; on the other hand, the greatest drag reduction was obtained with the combination of polymer with bubble for 272 ppm, also shown were the average velocity fields (in units of the international system and in units of the wall) and the average deformation maps (dimensionless) for the different working conditions, as well as the values of the shear stress in the wall, the friction velocity and a study of the average deformation in the damping sublayer (y+ = 7 = 0. 48mm) for the critical conditions water with polymer and water with bubbles - polymer both for 272 ppm compared to the solvent without drag reducing additives, which justified the drag reduction values obtained for those conditions.

Experimental setup

The technique that was used to carry out the experimentation is particle image velocimetry (PIV), which is a technique used to obtain instantaneous velocity fields.

ISSN 2524-2121

The camera used in this experiment is Megaplus ES 1.0, which can capture 30 images per second, with a resolution of 1008 x 1018 pixels. The laser used is an Nd:YAG, which produces through an optical array a sheet of light with a length of 532 nm (green color) and an energy per pulse of 32 mJ (see Figure 1).

.

Figure 1 Photograph of the experimental setup

Figure 2 shows the channel with dimensions (2cm x 10cm x 160cm), where the experimental tests were performed and through which water was passed with an inlet flow of 15 lpm and using the hydraulic diameter ($D_{Hydraulic}$) the average velocity was calculated with equation 3 and substituting in equation [6] the Reynolds number (Re) is obtained.

$$Re = \frac{\rho X \bar{u} X D_{\text{Hydraulic}}}{\mu} = 5200 \qquad (6)$$

Figure 2 also shows test zone 3, where the flow is fully developed and therefore the velocity measurements were carried out there. On the other hand, test zone 1 is also shown, in which it was calculated that 66 pix correspond to 1 mm and the time between photographs ($t_{adjustment}$) is calculated by means of equation 7.

$$\text{tadjustment} = 1x10^6 \text{ x} \frac{0.25 \; x \; I_{AI}}{f_{px} \; x \; \bar{u}} \qquad (7)$$

Where: I_{AI} is the size of the interrogation area, f_{px} is the equivalent of a pixel in millimeters, $\bar{u}$ is the average flow velocity and 0.25 is the minimum distance that a particle of the interrogation area must travel.

It is substituted into equation 7.

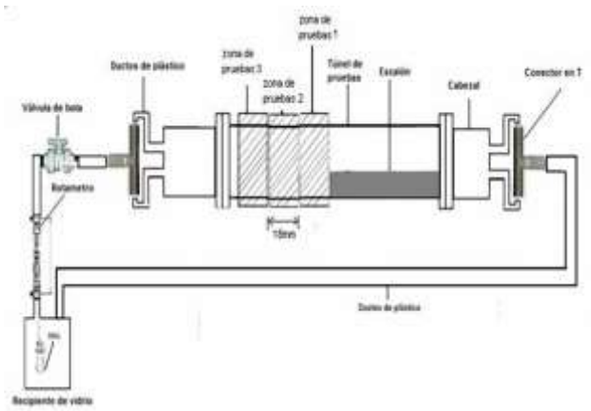

Figure 2 Experimental setup

In this way it was determined that the time between photographs should be 1100µs. A photograph of test area 3 can be seen in Figure 4.

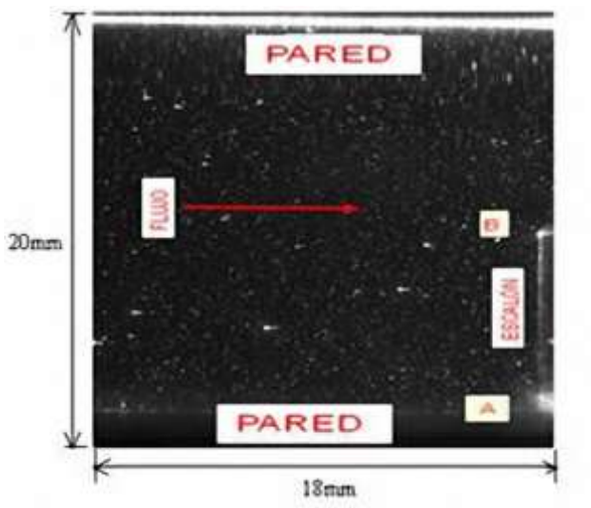

Figure 3 Experimental setup

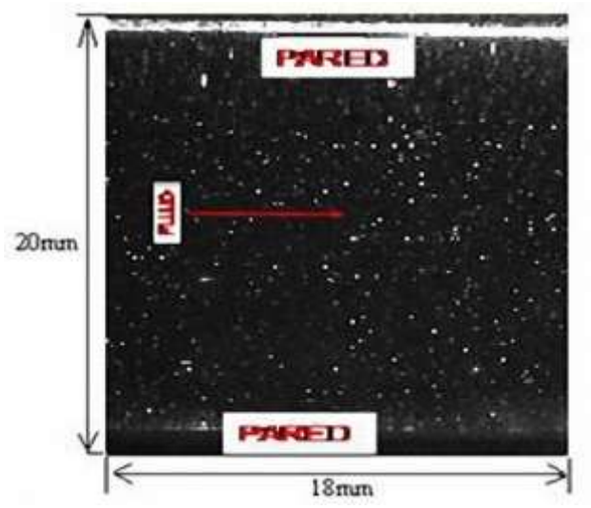

Figure 4 Experimental setup

Figure 5 shows the test matrix in which it is indicated that first we worked with water (without external agents), then we added bubbles (d = 10µm), cationic surfactant (sulfate-free shampoo) and polymers in concentrations of 164 and 272 ppm independently and finally we made the combinations of bubbles with polymers, bubbles with surfactants and polymers with surfactants also for the concentrations of 164 and 272 ppm.

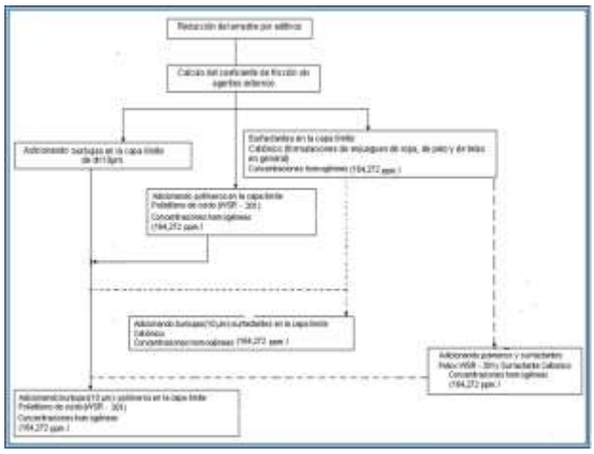

Figure 5 Test Matrix

On the other hand, the bubbles were produced by electrolysis and the electrical conductor was a thin copper wire of 10 µm diameter, fed by a voltage source of 20 Volts direct current. The power supplied to the circuit was set to a maximum value of 0.354W, to avoid significant corrosion effects on the cathode.

The average diameter of the hydrogen bubbles obtained was approximately 10µm. Figure 6 shows a velocity contour, which was modeled with the Fluent version 5.6 computational software, where it can be seen that at approximately 130 diameters (16cm) of the wire in the direction of the free current, the velocity gradients are no longer affected by it (Alejandro Alonzo Garcia, 2009). This allowed us to conclude that by placing the wires at 20cm from the test area, the disturbances induced by their presence will be significantly minimized.

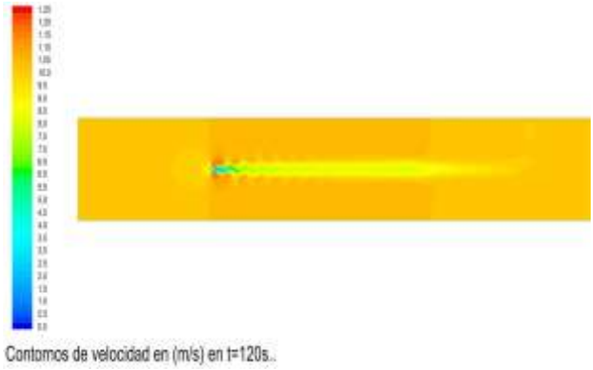

Figure 6 Contour Map [15]

Table [1] shows the experimental matrix in the first column shows the number of Re, in the second column shows the working conditions for 1 phase, which refers to the solvent (water) without drag reducing additives, 2 phases is when a drag reducing agent is added and three phases means that the mixtures bubbles with polymer, bubbles with surfactant and polymer with surfactant are added, on the other hand in column 3 is the electrical power consumed by the wire and in the last column the vacuum fraction.

Reynolds	Tests	Electrical power (W)	α (%)
5200	1 Phase	0	0
	2 Phases	0.782	0.782
	3 Phases	0.782	0.782

Table 1 Experimental matrix for bubles

$$\alpha = \frac{A_{burbujas}}{A_t} \quad (8)$$

The void fraction was calculated with equation 8 and in Figure 7 a photograph is shown, in which it can be seen that the bubbles and the tracer seeds give off a certain amount of light, when they pass through the PIV laser, then an application developed in Visual C++ software was used (the software was developed by A. Alonzo Garcia (Alejandro Alonzo Garcia, 2009)) was used to transform the light given off into an average grayscale value, which are 198 for the seeds and 255 for the bubbles and in this way the number of bubbles that were injected can be estimated and because the diameter of the bubbles is known the area occupied by the bubbles can also be calculated.

ISSN 2524-2121

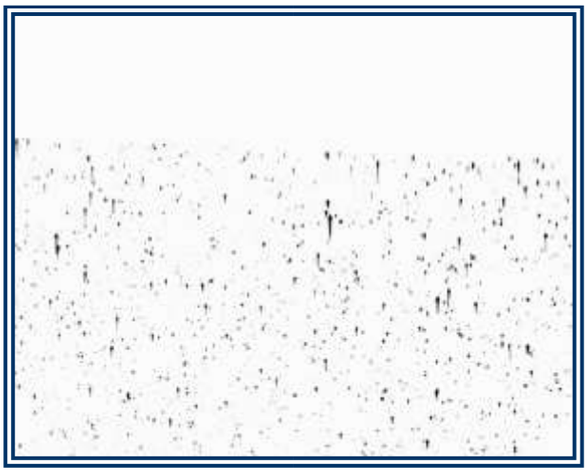

Figure 7 Bubbles obtained from the filtration process

Experimental results of properties of the mixtures of water with polymer and water with its surfactant

There is a possibility that the addition of polymers and surfactants in the working fluid (water) may alter the viscosity and density, for this reason it was decided to perform experimental measurements of water-polymer and water-surfactant solutions with a pycnometer (5 ml) and a viscometer.

Table 2 shows the values of density and absolute and kinematic viscosities of the polymer-water solution mixed by hand with water replacement (the solvent is replaced for each working condition) and Table 3 without water replacement (the solvent is not replaced for each working condition), while Table 4 shows the values with water replacement but mixing the solution with a blender and Table 5 also uses a blender but without water replacement.

PPM	Density (g/ml)	Dynamic Viscosity (cp)	Viscosity Kinematic (cst)
0	0.998	1	1.002
300	1.040	0.955	0.918
500	1.010	0.958	0.949
800	1.008	0.981	0.973
1000	1.024	1.002	0.979
1500	1.002	1.012	1.010
2000	1.030	1.02	0.990

Table 2 Property values of the hand-mixed polymer-water solution with water replacement for different concentrations

PPM	Density (g/ml)	Dynamic Viscosity (cp)	Viscosity Kinematic (cst)
0	0.998	1	1.002
300	1.008	0.956	0.948
500	1.011	0.957	0.947
800	1.012	1.006	0.994
1000	1.002	0.979	0.977
1500	1.008	1.065	1.057
2000	1.014	1.03	1.016

Table 3 Property values of the polymer-water solution mixed by hand without water replacement for different concentrations.

PPM	Density (g/ml)	Dynamic Viscosity (cp)	Viscosity Kinematic (cst)
0	0.998	1	1.002
300	1.007	1.022	1.015
500	1.005	1.023	1.018
800	1.012	1.043	1.031
1000	1.013	1.036	1.023
1500	1.016	1.03	1.014
2000	1.009	1.009	1.000

Table 4 Property values of the polymer-water solution mixed in a blender with water replacement for different concentrations

PPM	Density (g/ml)	Dynamic Viscosity (cp)	Viscosity Kinematic (cst)
0	0.998	1	1.002
300	1.008	1.030	1.022
500	1.015	1.039	1.024
800	1.010	1.042	1.032
1000	1.018	1.032	1.014
1500	1.022	1.022	1.000
2000	1.022	1.012	0.990

Table 5 Property values of the mixed polymer-water solution in blender without water replacement for different concentrations

Graph 1 shows the behavior of the absolute viscosity of the polymer-water solution with respect to the concentration in parts per million (ppm) of the additive for each condition, Graph 2 shows the kinematic viscosity and Graph 3 shows the density.

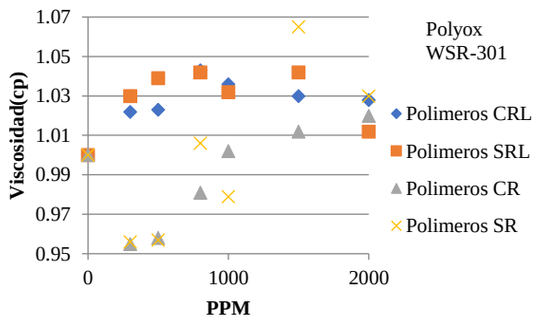

Graph 1 Absolute viscosity values of the polymer-water solution for different concentrations

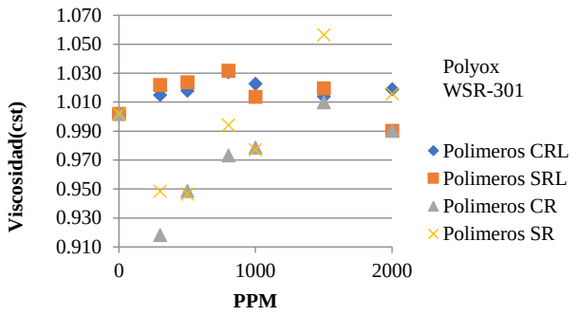

Graph 2 Values of the kinematic viscosity of the water-polymer solution for different concentrations.

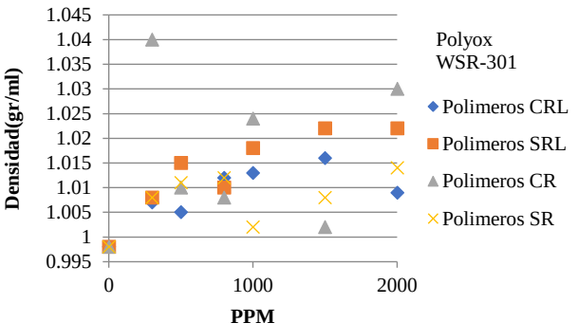

Graph 3 Values of the density of the water-polymer solution for different concentrations.

Graph 1 shows that the absolute viscosity of the water-polymer solution varies between 0.2% (where the solution is mixed by hand with water replacement and a concentration of 1000ppm) to 4.2% (where the solution is mixed in a blender without water replacement and for concentrations of 800 and 1500 ppm).

On the other hand, Graph 2 shows that the kinematic viscosity of the waterpolymer solution varies from 0.6% (where the solution is mixed by hand without water replacement and for a concentration of 800ppm) to 5% (where the solution is mixed by hand with water replacement and for a concentration of 500 ppm).

Finally, Graph 3 illustrates that the density of the water-polymer solution varies from 0.2% (where the solution is mixed by hand without water replacement and for a concentration of 1000ppm) to 4% (where the solution is mixed by hand with water replacement and for a concentration of 300 ppm).

Based on the above it can be said that the extreme lower and upper values of the properties (density and viscosities) of the water-polymer solution are given when it is mixed by hand and the most homogeneous values are given when it is mixed in a blender.

Table 6 shows the values of density and absolute and kinematic viscosities of the surfactant-water solution mixed by hand with water replacement and Table 7 without water replacement, while Table 8 shows the values with water replacement but mixing the solution with a blender and Table 9 also uses a blender but without water replacement.

PPM	Density (g/ml)	Dynamic Viscosity (cp)	Viscosity Kinematic (cst)
0	0.998	1	1.002
300	1.014	1.045	1.031
500	1.002	1.038	1.036
800	1.01	1.048	1.038
1000	1.01	1.026	1.016
1500	1.022	1.016	0.994
2000	1.018	1.016	0.998

Table 6 Property values of the surfactant-water solution mixed by hand with water replacement for different concentrations.

PPM	Density (g/ml)	Dynamic Viscosity (cp)	Viscosity Kinematic (cst)
0	0.998	1	1.002
300	1.001	1.02	1.019
500	0.995	1.026	1.031
800	0.995	1.027	1.032
1000	0.986	1.04	1.055
1500	0.98	1.026	1.047
2000	0.998	1.026	1.028

Table 7 Property values of the surfactant-water solution mixed by hand without water replacement for different concentrations

PPM	Density (g/ml)	Dynamic Viscosity (cp)	Viscosity Kinematic (cst)
0	0.998	1	1.002
300	1.011	1.045	1.034
500	1.006	1.040	1.034
800	1.007	1.007	1.000
1000	1.016	1.040	1.024
1500	0.991	1.043	1.052
2000	1.018	1.037	1.019

Table 8 Property values of the surfactant-water solution mixed in Blender with water replacement for different concentrations

ISSN 2524-2121

PPM	Density (g/ml)	Dynamic Viscosity (cp)	Viscosity Kinematic (cst)
0	0.998	1	1.002
300	1.024	1.032	1.008
500	1.021	1.011	0.990
800	1.02	0.995	0.975
1000	1.016	0.988	0.972
1500	1.017	1.031	1.014
2000	1.018	1.029	1.011

T**able 9** Property values of the surfactant-water solution mixed in blender without water replacement for different concentrations.

Graph 4 shows the behavior of the absolute viscosity of the surfactant-water solution with respect to the concentration in parts per million (ppm) of the additive for each condition, Graph 5 shows the kinematic viscosity and Graph 6 shows the density.

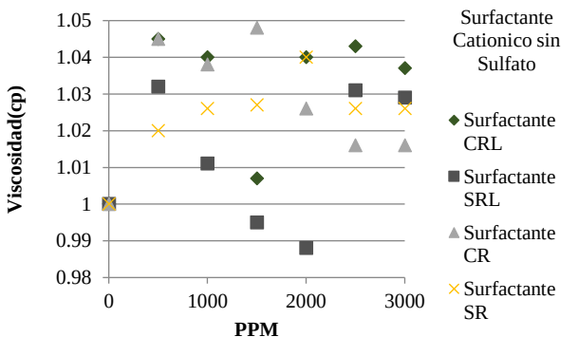

Graph 4 Values of the absolute viscosity of the water-surfactant solution for different concentrations.

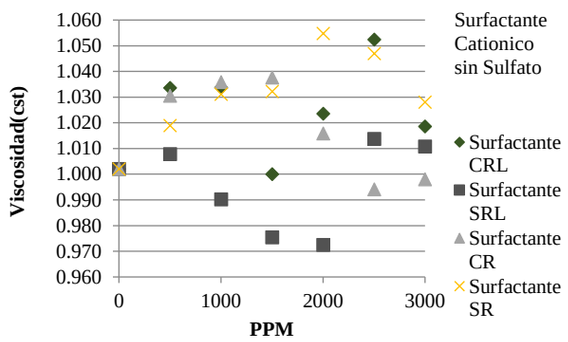

Graph 5 Values of the kinematic viscosity of the water-surfactant solution for different concentrations.

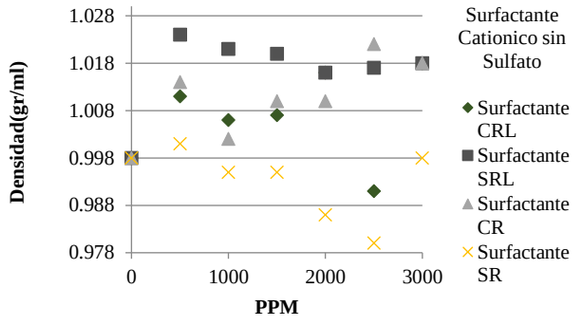

Graph 6 Values of the density of the water-surfactant solution for different concentrations

Graph 4 shows that the absolute viscosity of the water-surfactant solution varies from 0.5% (where the solution is mixed in a blender without water replacement and for a concentration of 1500 ppm) to 4.8% (where the solution is mixed by hand with water replacement and for a concentration of 1500 ppm).

On the other hand, Graph 5 shows that the kinematic viscosity of the water-surfactant solution varies from 0% (where the solution is mixed in a blender with water replacement and a concentration of 1500ppm) to 5% (where the solution is mixed by hand with water replacement and for a concentration of 2500 ppm).

Finally, Graph 6 illustrates that the density of the water-surfactant solution varies from 0.1% (where the solution is mixed by hand without water replacement and for a concentration of 500ppm) to 2.4% (where the solution is mixed in a blender without water replacement and for a concentration of 500ppm).
.

Based on the above it can be said that the lower and upper extreme values of the properties (density and viscosities) of the water-surfactant solution is not affected by the mixing method and is also not affected by the water replacement and for that reason it was decided to work in this experiment by mixing the polymers and surfactants without water replacement and blending them but the most important thing was that the densities and viscosities of the water-polymer and water-surfactant solutions are not affected by the mixing method and also not affected by the water replacement. polymer and water-surfactane solutions vary by less than 5% for all conditions with respect to water so the density and viscosity of water can be used in the data obtained.

ISSN 2524-2121

Experimental results for turbulent water flow with the addition of bubbles, polymer and surfactants

The average velocity profiles in International System units and in wall units, as well as the drag reduction and average deformation fields (dimensioned by multiplying by the hydraulic diameter DHydraulic and dividing by the local average velocity $\bar{u}$) in a turbulent water flow for a Re = 5200 with the addition of bubbles were determined, cationic surfactant (sulfate-free shampoo), polymers (polyox WSR301) and their combinations bubbles with polymers, bubbles with surfactants and polymers with surfactants for concentrations 164 and 272 ppm, in the horizontal center plane of test zone 3 of the channel.

The average velocity field presented in Figure 8 is averaged only with respect to time and in Figure 9 a small section (4 x 4 mm) of this same velocity field is presented so that the velocity vectors can be better appreciated and in Graph 7 it is shown averaged not only with respect to time but also with respect to space resulting in average velocity profiles in the fully developed flow region (test zone 3, which was tested with $\frac{du}{dx}$ ~0) temporally and spatially averaged for each work condition.

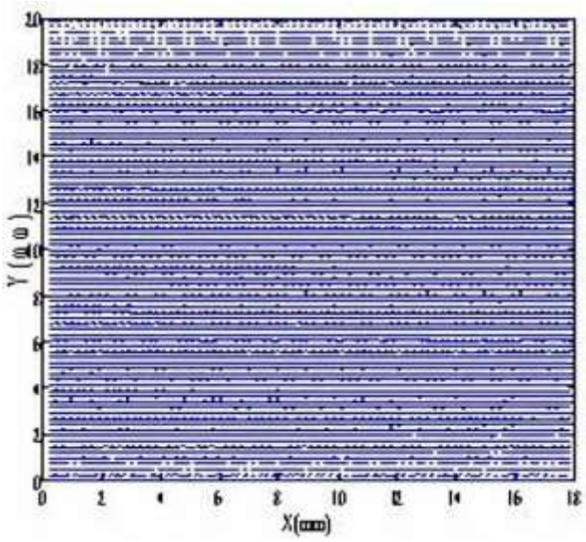

Figure 8 Averaging velocity field test zone 3

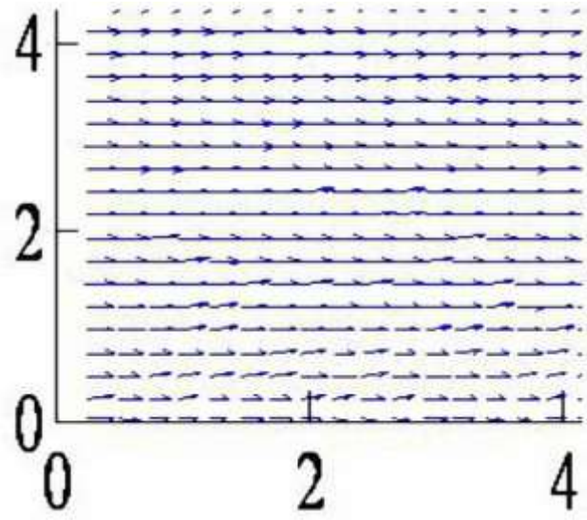

Figure 9 Trimmed average speed field test zone 3

It is evident that the velocity increases or decreases depending on the working condition. Taking as a parameter the velocity in the center of the channel, which is the maximum velocity (umax) that can be reached. Then, when working only with surfactants the umax increased 36.55 and 29.48 % for the concentrations of 164 and 272 ppm respectively, while when polymers were added the umax behaved differently, increasing 2.65% for 164 ppm and decreasing 4.73% for 272 ppm.

In the case of the bubbles there was an increase of 33.76% and in the combination of surfactant (sulfate-free shampoo) with bubbles there were considerable increases of 32.48 and 32.93% for 164 and 272 ppm respectively, on the other hand in the combinations of bubbles with polymers there were increases of 37.64 and 35.67% for the same concentrations.

Finally, for the combinations of polymer with surfactant, there were increases of 36.01 and 31.07 % also for 164 and 272 ppm as shown in Figure 8.

ISSN 2524-2121

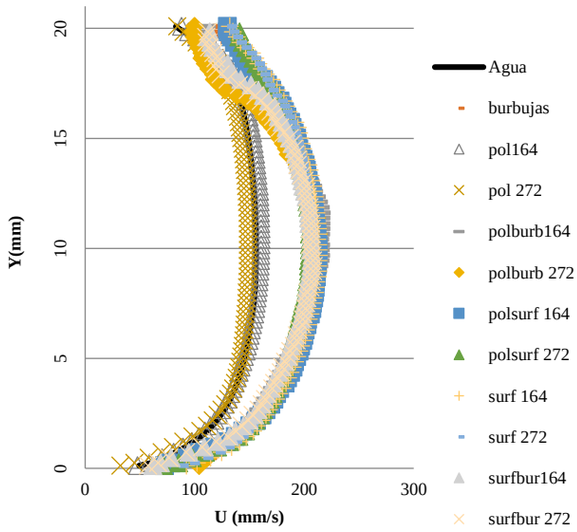

Graph 7 Average velocity profiles in the fully developed flow zone (test zone 3).

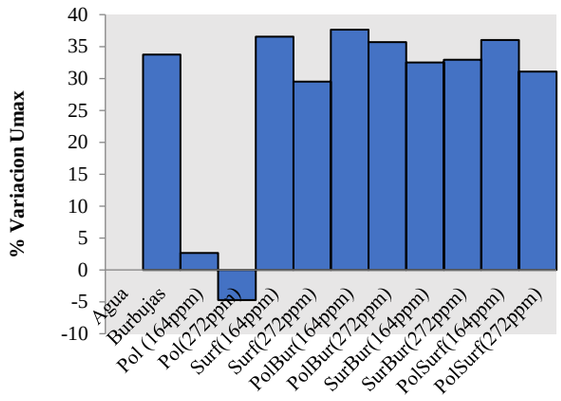

Graph 8 Variation of umax for each working condition.

The wall shear stresses and friction velocity were also calculated using the first order forward finite difference method for each working condition, then substituting the values obtained from the velocity profiles in Eqs. [9] and [10].

$$\tau wall = \mu \frac{du}{dy} \quad (9)$$

Where μ is the absolute viscosity of water (1cp), du/dy is the velocity gradient with respect to the distance from the wall.

$$u\tau = \sqrt{\frac{\tau_{wall}}{\rho}} \quad (10)$$

Where ρ is the density of the solvent (water).

Substituting in equation [11] the shear stress of the water wall with and without additives, the drag reduction percentages are obtained.

$$DR\% = \frac{\left|\tau_{water} - \tau_{additive}\right|}{\tau_{water}} X100 \quad (11)$$

Table 10 shows the values of shear stresses, friction velocities and drag reduction percentages for each condition. In which a drag reduction of 69.12% is shown for bubbles, for surfactants (sulfate-free shampoo) drag reductions were obtained for 164 and 272 ppm of 11.47 and 7.58% respectively, however for the case where polymers were added (Polyox WSR-301) there was only a reduction of 0.05% for 164 ppm, so it can be considered that there was no change in drag for that working condition and for 272 ppm there was an increase in drag of 15%, and in the case where polymers were added (Polyox WSR-301) there was only a reduction of 0.05% for 164 ppm, so it can be considered that there was no change in drag for that working condition, and for 272 ppm there was an increase in drag of 15%.

In the case where two techniques were combined, the greatest drag reductions for bubbles with surfactant were 37.36 and 16.16 % for 164 and 272 ppm, while for surfactants with polymers a drag reduction of 46.98 % was obtained for 164 ppm and an increase of 24.9% for 272 ppm, the best results in drag reduction were obtained with the combination of bubbles with polymers, which were 82.01 and 93.1 % also for 164 and 272 ppm. This is illustrated in Figure 9.

However, it is always important to dimension in order to compare the results, which was done by substituting the values of velocity and distance with respect to the wall in equations [12] and [13].

$$u^+ = \frac{u}{u_\tau} \quad (12)$$

$$y^+ = \frac{yu_\tau}{\nu} \quad (13)$$

	τ (N/m^2)	$u\tau$ (m/s)	DR (%)
Water	0.0914	0.0096	-
Bubbles	0.0282	0.0053	69.12
Surfactant(164PPM)	0.0809	0.0089	11.47
Surfactant(272PPM)	0.0845	0.0092	7.58
PolymeR (164PPM)	0.0913	0.00956	0.052
Polymer (272PPM)	0.1053	0.01026	-15.1
Surfburb(164PPM)	0.0573	0.0075	37.36
Surfburb(272PPM)	0.0766	0.0087	16.16
Surfburb(164PPM)	0.0164	0.0040	**82.01**
Polburb(272PPM)	0.0063	0.0025	**93.10**
Polsurf(164PPM)	0.0485	0.0069	46.98
Polsurf(272PPM)	0.1142	0.0107	-24.9

Table 10 Values of shear stress, friction velocity and drag reduction for bubbles and surfactants

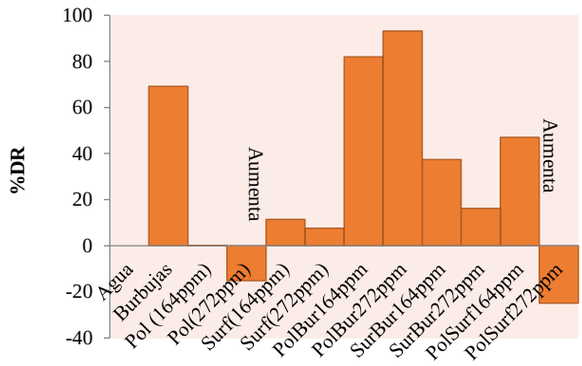

Graph 9 Variation of drag reduction in percentages for each working condition

Graph 10 shows the profiles in wall units, the profiles below the water profile indicate that the drag increases and above that it decreases.

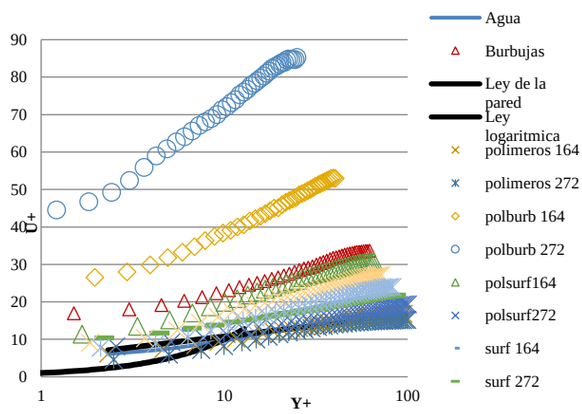

Graph 10 Velocity profiles in wall units

However, something that strongly calls the attention is what happened with the average deformation. In Figure [10], the average deformation field (dimensionless by multiplying by DHydraulic and dividing by $\bar{u}$) is illustrated for the condition without drag reducing agents and in the conditions where bubbles were independently added, cationic surfactant (sulfate-free shampoo) and polymers for 164 and 272 ppm.

Where it is seen that the average strain increases considerably from 2 to 3 times its value, while in the conditions where only polymers (polyox WSR-301) were added there is no considerable change in the average strain.

Figure 11 shows the deformation fields for the conditions where the combinations of bubbles with surfactants, bubbles with polymers and surfactants with polymers were added for the concentrations of 164 and 272 ppm, the deformation increased from 2 to 4 times its value. On the other hand, in the zone close to the wall, the deformation does not behave in the same way, unfortunately in the experiment presented it was not possible to visualize the viscous sublayer (y+ < 5), which is the zone closest to the wall, but according to Graph 10, the damping sublayer (5<y+ < 30) was visible.

Figure 12 shows the deformation field in both smooth curves and pixels (giving a matrix of 73 columns) in the near-wall zone (y < 2 mm) of the water without drag-reducing additives compared to the critical condition.

Where polymer was added for a concentration 272 ppm having a 15% increase in drag and Figure 13 also shows the comparison of water deformation in the same zone (and < 2 mm) with the condition, where bubbles were added with polymer for 272 ppm having a drag reduction of 93. 1%. These two critical conditions are supported by the values in Tables 11 and 12. Table 11 shows the strain values for the conditions where only polymer was added for 272 ppm, the values for water without additives and the difference of both conditions in the damping sublayer (y+ = 7 = 0. 484mm), which helps to know if the deformation increased or decreased with the drag reducing agent, if the difference gives us positive the drag decreases and if it gives us negative the drag increases, in this case the deformation values are shown in the row corresponding to y+ = 7 = 0.484mm (damping sublayer) and for the range from column 23 to 32, because in those points it is very well appreciated how the deformation increases and therefore that causes the drag to increase by 15%.

ISSN 2524-2121

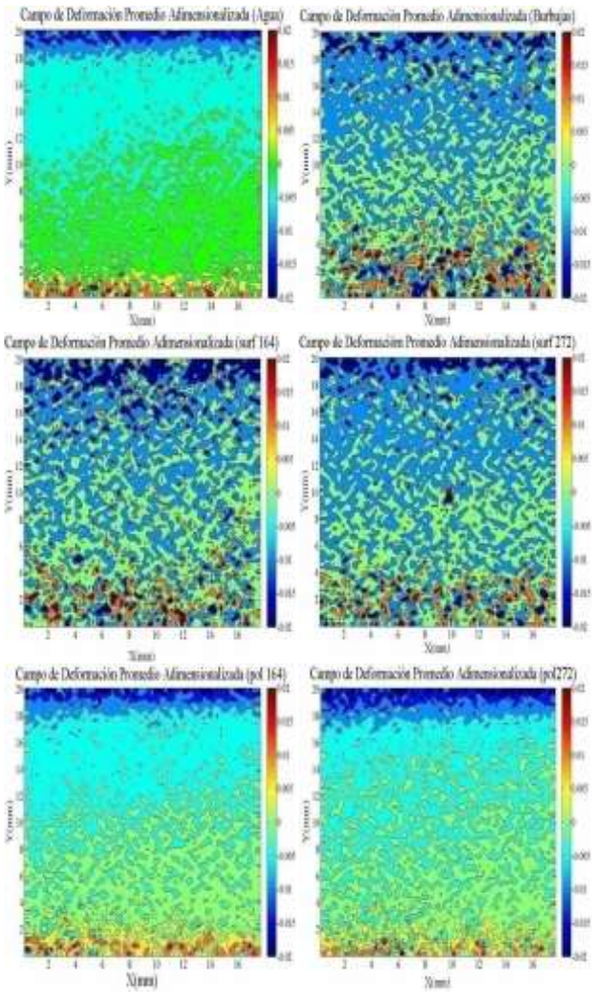

Figura 10 Campos de deformación para agua, surfactantes y polímeros para 164 y 272ppm.

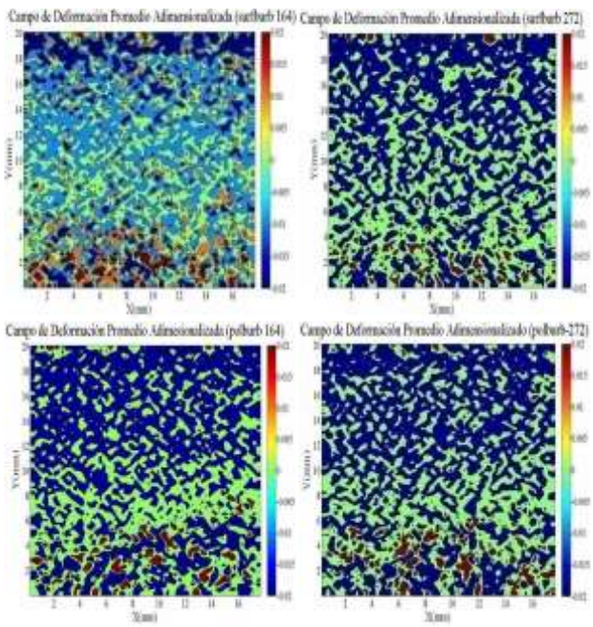

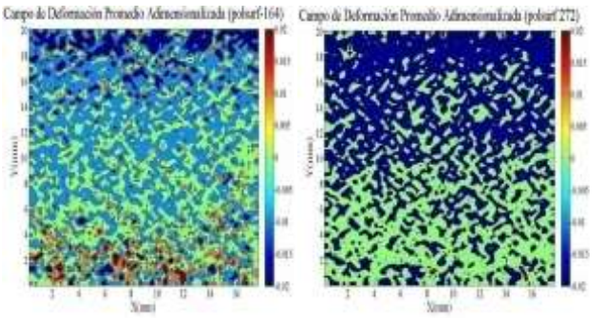

Figure 11 Deformation fields for bubble-polymers and bubble-surfactants (164 and 272 ppm)

On the other hand Table 12 shows the strain values for the combination of bubbles with polymers for 272 ppm compared to water and their difference were also carried out in the row corresponding to y+ = 7 = 0. 484mm but the range of the values shown is from column 38 to 48, but here most of the values obtained by subtraction of the absolute values of the water strain with the absolute values of the bubble with polymer condition are positive, which means that the strain decreased in the near-wall zone with the drag reducing agents and therefore that justifies that the drag was reduced by 91%.

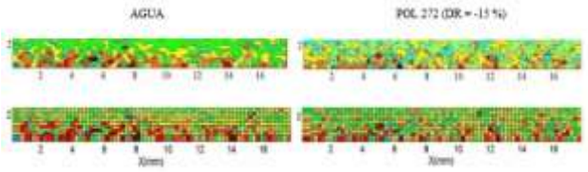

Figure 12 Comparison of Strain Fields for water and polymer at 272 ppm in the near-wall zone

Column	23	24	25	26	27
pol 272	-0.0190	-0.0176	-0.0115	-0.0162	-0.0190
Water	-0.0142	-0.0106	-0.0098	-0.0129	-0.0113
Difference	-0.0048	-0.0070	-0.0017	-0.0033	-0.0077
Condition	Increases	Increases	Increases	Increases	Increases
Column	28	29	30	31	32
pol 272	-0.0077	-0.0033	-0.0168	-0.0122	-0.0192
Water	-0.0131	-0.0183	-0.0162	-0.0145	-0.0044
Difference	0.0054	0.0150	-0.0006	0.0023	-0.0148
Condition	Decrease	Decrease	Increases	Decrease	Increases

Table 11 Strain values for water, polymer at 272 ppm, their difference and condition.

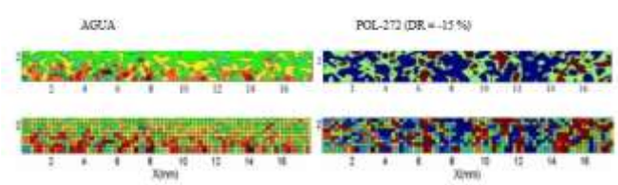

Figure 13 Comparison of Strain fields for water and bubbles with polymer at 272 ppm in the near-wall zone

ISSN 2524-2121

Column	38	39	40	41	42	43
polburb 272	0.006	-0.007	-0.015	-0.006	-0.027	-0.022
Water	0.011	-0.013	-0.018	-0.016	-0.014	-0.004
Difference	0.005	0.006	0.004	0.010	-0.013	-0.018
Condition	Decrease	Decrease	Decrease	Decrease	Increases	Decrease
Column	44	45	46	47	48	
polburb 272	-0.005	0.009	0.012	-0.011	-0.020	
Water	-0.008	-0.018	-0.015	-0.024	-0.018	
Difference	0.004	0.009	0.003	0.013	-0.002	
Condition	Decrease	Decrease	Decrease	Decrease	Increases	

Table 12 Strain values for water, polymer with water 272 ppm, their difference and condition

Table 13 shows the average strain values for all conditions at y+ = 7 = 0.48mm located in the buffer sublayer, which increased or decreased and were also compared with the drag reduction, for example for the conditions where bubbles, polymers, polymers with bubbles and polymers with surfactants were added for 164 ppm 46.57 % of the strain values increased and 53.42 % decreased giving 69.12, 0.052, 82.01 and 46. 98 % in drag reduction respectively, for the conditions where the surfactant with bubbles combinations are added for both 164 and 272 ppm 42.46 % of the values increase and 57.53 % decrease having a drag reduction of 37. 36 and 16.16 % and for the conditions where surfactants were added for 164 and 272 ppm 47 .94 and 45.89 % of the values increased and 52.05 and 54.1 % decreased respectively, while in the case of bubbles 46.57 % increased and 53.42 % decreased.

It is evident that in all the above mentioned conditions there was a higher percentage of the average strain values that decreased to those that increased when compared to the condition where no drag reducing agents were worked. On the other hand in the cases where the drag increased the percentage of the strain values decreasing is lower than those increasing when compared to the solvent (water) values for example for the condition where polymer was added independently for 272 ppm there was an increase in drag reduction of 15 % due to 72. 6 % of the strain values increased and only 27.39 % decreased and finally for the condition where polymer was added with surfactant for 272 ppm 57.53 % of the strain values increased and 46.46 % decreased, therefore there was an increase of 24.9 % of the drag.

Condition	Increases (%)	Decreases (%)	DR (%)
Bubbles	46.57	53.42	69.12
Surfactant(164ppm)	47.94	52.05	11.47
Surfactant(272ppm)	45.89	54.1	7.58
Polymer (164ppm)	46.57	53.42	0.052
Polymer (272ppm)	72.60	27.39	-15.1
SurfBurb(164ppm)	42.46	57.53	37.36
SurfBurb(272ppm)	42.46	57.53	16.16
PolBurb(164ppm)	46.57	53.42	**82.01**
PolBurb(272ppm)	45.20	54.79	**93.10**
PolSurf(164ppm)	46.57	53.42	46.98
PolSurf(272ppm)	57.53	46.46	-24.9

Table 13 Percentages of strain values increasing or decreasing at y+ = 7 =0.48 mm for different working conditions

Acknowledgement

We thank the Laboratory of Applied Hydraulics and Applied Hydraulics LAMINTHAP for the facilities provided for the experimentation.

Funding

This work has been funded by the Secretary of Research and Graduate Studies through project SIP 2021079 of the National Polytechnic Institute.

Conclusions

The average velocity profiles and also the average deformation fields were determined for each condition, where it was observed that when drag reducers were added, the velocity and deformation did not have a tendency, which was demonstrated in the maximum velocity variation graphs and in the deformation fields. When drag reducing agents were added, bubbles, surfactants, polymers and the combinations bubbles with surfactants, bubbles with polymers and surfactants with polymers, the velocity increased considerably from 30% to 38%. However, when only polymers were added the maximum velocity increased less than 3% for 164 ppm and increased 5% for 272 ppm.

On the other hand, the average deformation in the far wall zone (y > 2 mm) increased by 2 to 3 times when only cationic surfactant (sulfate-free shampoo) was added, contrary to what occurred when only polymers were added, where it can be considered that the deformation fields did not change considerably with respect to the polymer condition.

ISSN 2524-2121

When bubbles or their combinations were used with the concentrations 164 and 272 ppm of surfactant (sulfate-free shampoo) in the same zone far from the wall (overlapping sublayer and outer sublayer) increased from 2 to 4 times.

However, in the zone close to the wall and < 2mm (viscous and buffer sublayer) the deformation did not behave in the same way as in the zone far from the wall (overlap sublayer and outer sublayer) because although there is no trend, it could be seen in Table 13 that the deformation decreases when the drag reduction increases. This is logical because the shear stress also decreases, for example, in the conditions where the highest percentages of drag reduction were obtained, which were when bubbles and polymers with bubbles were added for 164 and 272 ppm, it can be seen that the deformation at the point y+ = 7 = 0. 48mm decreases between 53 to 55 %.

However, it is possible that the reason why a trend was not found was because the results shown in Table 13 belong only to a point in the damping sublayer and also the viscous sublayer could not be appreciated, so it is recommended to make a more thorough study of the near-wall region especially of the viscous and damping sublayers since it is possible that the reduction of the deformation in that area explains the reduction of the drag so high obtained under these conditions.

When only bubbles were used, there was a considerable increase in the drag reduction of 70% and the combinations of bubbles with polymers (polyox WSR - 301) had the best results in drag reduction of 82 and 93% for the concentrations of 164 and 272 ppm respectively, while when combinations of bubbles with surfactants were used, the results were 37 % for 164 ppm and only 16 % for 272 ppm, and for the combination of polymer with surfactant for 164 ppm the results were 47 % and for 272 ppm the drag increased by 25 %, possibly due to an incorrect preparation of the polymer or surfactant.

Therefore, it is concluded that the greatest synergistic benefit is presented when combining the bubble drag reducer and polymer techniques, which consists of the fact that the polymers (polyox WSR - 301) break the surface tension and this facilitates the injection of the bubbles in the buffer sublayer and in turn the bubbles contribute to the polymers to be transported in an orderly manner in the area near the wall, therefore both techniques help each other. But it is necessary to make an energy study since it must be considered that the addition of bubbles (injected by electrolysis) and polymers consumes more energy than the addition of only one, and it will be necessary to see if more energy is saved than consumed when both techniques are used.

Nomenclature

A	Cross-sectional area of the channel [m2].
D	Microbubble diameter [μm].
DHydraulic	Hydraulic Diameter of the channel [m] [m] [m
DR%	Percentage of drag reduction [%] [%] [%]
	Friction coefficient
F	Friction coefficient
f_S	Solution friction coefficient
f_N	Coefficient of friction of solvent without friction reducing agents
fpx	Pixel equivalence in millimeters
G	Acceleration due to gravity
IAI	gravity [m/s2] [m/s2
PIV	Size of interrogation area
pol 164	interrogation area size [pix]
pol 272	Image velocimetry of
polburb 164	particles
polburb 272	polymer at 164 ppm concentration
Ppm	polymer at 272 ppm concentration
ΔP_S	polymer with bubbles at 164 ppm concentration
Surf 164	Polymer with bubbles at 272 ppm concentration
surf 272	parts per million
surfburb 164	Solution pressure drop
surfburb 272	Surfactant at τwater concentration 164 ppm
surfpol 164	surfactant at τpared concentration 272 ppm
surfpol 272	Surfactant-bubble combination for a concentration of 164ppm
tajuste	bubble for a concentration of 164ppm
u^+	Surfactant-bubble combination for a concentration of 272ppm
u_τ	bubble for a concentration of 272ppm
$\bar{u}$	Surfactant-polymer
umax	polymer for a
X	concentration of 164ppm
Y	Surfactant-polymer combination
y+	polymer for a
Z	concentration of 272ppm

ISSN 2524-2121

References

A.Gyr, H.W. Bewersdorff. (1995). Drag Reduction of Turbulent Flows by Additives. En A. a. Bewersdorff, *Drag Reduction of Turbulent Flows by Additives* (Vol. 32, págs. 69-99). Springer Link. Recuperado el 1995

Alejandro Alonzo Garcia. (2009). Estudio mediante la tecnica de PIV de lo efectos de la presencia de microburbujas dentro de la cpa limite turbulenta. *TESIS ALEJANDRO ALONZO GARCIA*. Mexico: Instituto Politécnico Nacional.

Dongjie Liu un, , Qinghui Wang unJinjia Wei. (2018). Estudio experimental sobre el rendimiento de reducción de arrastre de soluciones mixtas de polímeros y surfactantes. *Investigacion y Diseño en Ingenieria Quimica, 132*, 460-469. doi:https://doi.org/10.1016/j.cherd.2018.01.047

Ferhat Hadri, Sylvain Guillou. (2010). Reducción de arrastre por tensioactivo en cerrado flujo turbulento. *Revista Internacional de Ciencia y Tecnología de Ingeniería*, 6876-6879. doi:ISSN: 0975-5462

George H. Choueiri, José M López, Björn Hof. (23 de Marzo de 2018). Exceder el límite asintótico de la reducción de arrastre del polímero. *Phys Rev Lett*. doi:10.1103/PhysRevLett.120.124501

Lucas Warwaruk, Sina Ghaemi. (21 de abril de 2021). Una comparación directa de la turbulencia en flujos reducidos por arrastre de polímeros y tensioactivos. *Revista de Mecánica de Fluidos, 197*. doi:https://doi.org/10.1017/jfm.2021.264

Lumley, J. L. (1969). Drag Reduction by Additives. *Journal Fluid Mechanics, 1*, 367-384.

M. A. Asidin, E. Suali, T. Josnukin, F. A. Lahin. (8 de Agosto de 2019). Revisión de las aplicaciones y desarrollos del polímero reductor de arrastre en el flujo de tuberías turbulentas. *Revista china de ingeniería química, 27*, 1921-1932. doi:https://doi.org/10.1016/j.cjche.2019.03.003

Toms, B. (1948). Some Information on the Flow of linear Polymer Through Straight Tubes at Large Reynolds Number. *Proc. 1st. int. cong. on Rheology, Pt2*, (págs. 135-141). North Holland Amesterdam.

Weichi Gang, Jun Shen, Wei Dai, Ke Li, Maoqiong Gang. (2021). Research and Aplications of Drag Reduction In Thermal Equipment. *International Journal Of Heat and Mass Transfer, 72*. doi:https://doi.org/10.1016/j.ijheatmasstransfer.2021.121152

White, F. (2008). Fluid Mechanics. En F. White, *Fluid Mechanics* (Sixth ed., págs. 483-486). Prentice Hall.

Xiaoping Li, Jiaxin Pan 1Jinwen Shi, Yanlin Chai, Songwei Hu, Qiaorong Han, Yanming Zhang, Xianwen Li, Dengwei Jing. (Abril de 2023). Reducción de arrastre inducida por nanopartículas para poliacrilamida en flujo turbulento con altos números de Reynolds. *Revista china de ingeniería química, 56*, 290-298. doi:https://doi.org/10.1016/j.cjche.2022.07.015

Xin Zhan, Xiaodong Dai, Jishi Zhao, Dengwei Jing, Fei Liu, Lei Li, Yanping Xin, Kun Liu. (27 de Septiembre de 2021). Predicción precisa de la eficiencia de reducción de arrastre del polímero en flujo turbulento considerando el efecto de diámetro. *Fisica de Fluidos*. doi:https://doi.org/10.1063/5.0065193

Yanuar, Sealtial Mau, Kurniawan T. Waskito, Okky A. Putra,Rifqi Hanif. (2017). Reducción de arrastre de nanofluido de alúmina en tubería en espiral con condiciones de flujo turbulentas. *Internacional de Energía Renovable Tropical* (pág. 1826). Bogor, Indonesia: TECNOLOGÍA E INNOVACIÓN EN ENERGÍAS RENOVABLES PARA EL DESARROLLO SOSTENIBLE:. doi: https://doi.org/10.1063/1.4979237

Ying Yuan; Jiaqiang Jing; Ran Yin; Peiyu Jing; Jianfei Hu. (11 de Mayo de 2022). Investigación experimental sobre tensioactivos catiónicos en la reducción de arrastre de tuberías de inyección de agua. *SPE Prod & Oper, 37*, 331-345. doi:https://doi.org/10.2118/209593-PA

Article **ECORFAN Journal- Taiwan**
June, 2023 Vol.7 No.13 32-38

Comparison and interpretation of solarimetric station data (diffuse solar radiation, UVB radiation, temperature, and relative humidity) from January 2017 to November 2018 in Zacatecas

Comparación e interpretación de los datos de la estación solarimétrica (radiación solar difusa, radiación UVB, temperatura y humedad relativa) del periodo enero 2017 a noviembre 2018 en Zacatecas

BERLANGA-MORENO, Edgar Darío†, GARCÍA-GONZÁLEZ, Juan Manuel*, GONZÁLEZ-CABRERA, Adriana Elizabeth and VILLEGAS-MARTÍNEZ, Rodrigo Cervando

Universidad Autónoma de Zacatecas. Unidad Académica de Ciencias QuímicasUniversidad Nacional Autónoma de México. Instituto de Geofísica.

ID 1st Author: *Edgar Dario, Berlanga-Moreno* / **ORC ID:** 0009-0002-2026-3644

ID 1st Co-author: *Juan Manuel, García-González* / **ORC ID:** 0000-0001-7259-5021, **CVU CONAHCYT ID:** 346241

ID 2nd Co-author: *Adriana Elizabeth, González-Cabrera* / **ORC ID:** 0000-0003-2802-6811

ID 3rd Co-author: *Rodrigo Cervando, Villegas-Martínez* / **ORC ID:** 0000-0003-0474-6734

DOI: 10.35429/EJT.2023.13.7.32.38 Received March 22, 2023; Accepted June 11, 2023

Abstract

In this research work, the data from the solarimetric station in Zacatecas during the period from January 2017 to November 2018 are compared and interpreted. The main objective is to analyze the climate and solar radiation characteristics in the region and identify possible correlations between variables. The methodology involved data collection using the solarimetric station and data processing in Excel. Hourly,daily, and monthly averages were calculated for diffuse solar radiation, UVB radiation, temperature, and relative humidity. In addition, graphs were generated using Excel,and two R codes were developed: one to obtain correlations among the analyzed variables and another to visualize the UVB index. This study provides a detailed analysis of climate data and solar radiation patterns in Zacatecas. The obtained results are relevant for the design and implementation of solar energy systems in the region and in areas with similar climatic conditions. In summary, this study compares and interprets the datafrom the solarimetric station in Zacatecas, aiming tounderstand the climate and solar radiation characteristics. The conducted analyses contribute to the development ofsolar energy strategies in Zacatecas and similar regions. solar radiation, climate analysis, Zacatecas.

Solar Radiation, Climate, Correlations

Resumen

En este trabajo de investigación, se comparan e interpretan los datos de la estación solarimétrica de Zacatecas del periodo de enero 2017 a noviembre 2018. El objetivo principal es analizar las características del clima y la radiación solar en la región, para identificar posibles correlaciones entre variables. La metodología se basó en la recopilación de datos mediante la estación solarimétrica y procesamiento en Excel. Se calcularon promedios horarios, diarios y mensuales de la radiación solar difusa, la radiación UVB,la temperatura y la humedad relativa. Además, se generaron gráficos utilizando Excel y se desarrollaron dos códigos en R: uno para obtener correlaciones entre las variables analizadas y otro para visualizar el índice UVB. Este trabajo ofrece un análisis detallado de los datos climáticos y patrones de radiación solar en Zacatecas. Los resultados obtenidos son relevantes para el diseño y la implementación de sistemas de energía solar en laregión y en áreas con condiciones climáticas similares. En resumen, este estudio compara e interpreta los datos de la estación solarimétrica de Zacatecas, con el objetivo de comprender las características del clima y la radiación solar. Los análisis realizados contribuyen al desarrollo de estrategias de energía solar en Zacatecas y regiones similares.

Radiación Solar, Clima, Correlaciones

Citation: BERLANGA-MORENO, Edgar Darío, GARCÍA-GONZÁLEZ, Juan Manuel, GONZÁLEZ-CABRERA, Adriana Elizabeth and VILLEGAS-MARTÍNEZ, Rodrigo Cervando. Comparison and interpretation of solarimetric station data (diffuse solar radiation, UVB radiation, temperature, and relative humidity) from January 2017 to November 2018 in Zacatecas. ECORFAN Journal-Taiwan. 2023. 7-13: 32-38

* Author's Correspondence (e-mail: jmgarcia@uaz.edu.mx)
† Researcher contributing as first author.

Introduction

In this research, a comprehensive comparative and interpretative analysis of the data collected at the solarimetric station located in Zacatecas during the period from January 2017 to November 2018 is carried out. The fundamental purpose of this study is to discern the complex characteristics of climate and solar radiation in that region, with a special focus on exploring possible correlations between the variables analysed.

A thorough understanding of the climatic conditions and solar radiation in a specific locality is of paramount importance in view of its profound impact on multiple sectors, such as agriculture, renewable energy and public health. This analysis encompasses a holistic perspective by integrating multiple climatic variables, thus surpassing other one-dimensional techniques that are limited to solar radiation or a single climatic aspect.

This study delves clearly and precisely into each of the characteristics under investigation, examining in detail the temporal and spatial variability of diffuse solar radiation, UVB radiation, temperature and relative humidity, with the aim of identifying patterns and interdependent relationships between them.

The problem addressed in this research focuses on the study of the interconnections between the various climatic variables analysed. Our central hypothesis postulates the existence of significant correlations between these variables. Therefore, through the careful analysis and interpretation of the data collected, we seek to validate or refute this hypothesis, which will lead to a better understanding of the intricate relationship between climate and solar radiation in this specific region.

The structure of the paper is organised into carefully delineated sections, which provide a thorough and rigorous exposition of the results and conclusions obtained. Through this methodical approach, we aim to provide new knowledge that can be applied to the development of solar energy strategies both in Zacatecas and in other regions that share the same characteristics as well as in other regions sharing similar climatic characteristics.

Solarimetric station

A solarimetric station is an infrastructure used to measure solar radiation at a given location. These stations measure various parameters related to solar radiation, such as global solar radiation, direct solar radiation and diffuse solar radiation. In Mexico, several solarimetric stations have been installed in different parts of the country as part of a network of stations that is part of the Consorcio Centro Mexicano de Innovación en Energía Solar, coordinated by UNAM through the Instituto de Energías Renovables and financed by the Ministry of Energy. These stations make it possible to evaluate the potential of solar energy in different regions of the country and are an important tool for the study of climate change and the development of renewable energy projects.

Variables analysed

Diffuse radiation: Diffuse radiation is a component of solar radiation that is scattered in the atmosphere and reaches the earth's surface in all directions. Unlike direct radiation, which comes from the sun in a straight line, diffuse radiation is reflected by clouds, air and other surfaces before reaching the earth's surface. [I].

Ultraviolet B radiation: Ultraviolet B radiation (UVB) is a type of electromagnetic radiation present in sunlight. Unlike UVA radiation, UVB radiation has a shorter wavelength and is largely absorbed by the ozone layer before reaching the earth's surface. Excessive exposure to UVB radiation can have detrimental health effects such as sunburn, premature skin ageing and skin cancer. It is essential to take precautions to protect against UVB radiation, such as applying sunscreen, wearing protective clothing and avoiding prolonged exposure to the sun during peak hours of solar radiation [II], [III].

Ambient temperature: Ambient temperature refers to the temperature of the air surrounding a specific object or location.

It represents the amount of thermal energy present in the air in a given area and can vary according to various factors, such as time of day, season, geographic location and environmental conditions. This temperature has significant impacts on living beings and structures, such as pavements, as well as on the structural behaviour of roads.

ISSN 2524-2121

In addition, ambient temperature can influence the blood pressure of animals, including dogs. In certain cases, the increase in ambient temperature may be related to the greenhouse effect phenomenon, both natural and anthropogenic, which may have adverse consequences for the environment and human health [IV], [V], [VI].

Relative humidity: Relative humidity is defined as the proportion of water vapour present in the air relative to the maximum amount it could contain at a specific temperature. It is expressed as a percentage and is used to characterise the sensation of humidity in the atmosphere. In the field of meteorology, relative humidity plays a key role as it can influence cloud formation, precipitation and thermal perception. In addition, relative humidity can affect various materials [VII].

Methodology to be developed

The methodology used in this research was based on a rigorous and precise scientific approach to the analysis of the data collected from the solarimetric station in Zacatecas. In order to examine and understand the characteristics of climate and solar radiation in the region, a series of steps were followed and specialised instruments and software were employed. These elements allowed for a detailed analysis and meaningful interpretation of the data, which contributed to the Mexican solarimetric network.

Data collection: Data collection from the solarimetric station in Zacatecas was carried out during the period from January 2017 to November 2018. These data comprised measurements of diffuse solar radiation, UVB radiation, temperature and relative humidity.

Data transfer and organisation: The collected data were transferred to Excel spreadsheets, where they were organised and prepared for further analysis. Columns were created for the variables of interest and data were entered accurately.

Calculation of temporal averages: Using the capabilities of Excel, hourly, daily and monthly averages were calculated for each of the variables analysed. These averages provided an overview of the temporal patterns and trends of the variables studied and were subsequently plotted in the same software.

Data visualisation: after data analysis and interpretation, graphs and tables were produced in Excel. These analyses provided a visual representation of the data and allowed a preliminary assessment of the characteristics of climate and solar radiation in the study region.

Use of R for advanced statistical analyses: The R programming language was used to carry out more advanced statistical analyses. Two different codes were developed in R: one to calculate correlations between the variables studied and another to generate customised UVB index graphs, using colours to highlight different levels of intensity.

Interpretation of results: The results obtained from the data analysis were interpreted and critically analysed. Patterns, trends and significant relationships between the variables studied were identified, and relevant comparisons and conclusions were made about the characteristics of climate and solar radiation in the Zacatecas region

Results

Month	Diffuse radiation W/m²		Radiation UVB MED/h		Temperature°C		Relative humidity%	
	highest value	Day	highest valu	Day	highest valu	Day	highest value	Day
January	488.32	22	3.30	29	18.00	4	97.57	8
February	274.88	8	4.05	28	18.48	11	63.59	19
March	594.47	19	4.40	29	19.72	22	71.41	9
April	309.55	6	4.64	30	21.21	22	46.72	12
May	291.90	18	4.64	7	23.78	27	52.84	30
June	287.74	10	4.68	27	23.54	17	72.97	27
July	303.26	2	4.51	19	20.50	31	81.09	13
August	312.84	18	4.45	11	20.87	5	86.85	31
September	276.19	2	4.55	9	19.54	16	89.35	6
October	263.03	10	3.89	3	18.45	22	84.66	4
November	238.67	31	2.93	1	19.86	8	66.23	1
December	207.93	14	2.43	13	17.71		89.70	18, 24

Table 1 Months and days with the highest values of diffuse radiation, UVB radiation, ambient temperature and relative humidity in 2017
Own Elaboration

Table 1 shows the day with the highest value for each month of 2017 for each of the variables analysed. It can be seen that the diffuse radiation values for each month do not coincide with the number of days for the other properties measured. It can also be seen that on the 18th day of May and August the diffuse radiation was the highest of those two months, with the 19th of July being the day with the highest UVB radiation and the 22nd of March, April and October with the highest temperatures of each month respectively, finally the month of December had two days 18 and 24 with the same relative humidity which were the highest of the month.

ISSN 2524-2121

Month	Diffuse radiation W/m²		Radiation UVB MED/h		Temperature °C		Relative humidity %	
	highest value	Day	highest valu	Day	highest valu	Day	highest valu	Day
January	251.60	31	2.78	30	14.20	9	88.15	29
February	242.43	7	3.66	24	18.09	16	84.37	9
March	194.43	2	4.35	15	20.55	26	50.15	30
April	540.78	12	4.44	29	20.45	26	59.22	11
May	304.65	13	4.45	19	25.93	31	70.18	7
June	295.53	21	4.30	16	24.07	1	82.19	13
July	307.62	30	4.07	17	22.10	25	72.30	10
August	265.45	6	4.25	2	19.84	18,24	87.03	13
September	436.95	30	4.17	28	18.80	5	95.31	12
October	502.20	3	3.77	9	18.73	13	86.61	21
November	241.49	1	2.89	3	14.15	2	52.14	2

Table 2 Months and days with the highest values of diffuse radiation, UVB radiation, ambient temperature and relative humidity in 2018, prepared by the authors

Table 2 shows the day with the highest value for each month in 2018. It is noticeable that the diffuse radiation values for each month do not coincide in the number of days of the other properties measured, as in 2017. It can also be seen that on the 30th day of the months July and September the diffuse radiation was the highest of those two months, and on the 18th and 24th day of the month the diffuse radiation was the highest of those two months

Month	Radiation diffuse (W/m²)	Relative humidity (%)	UVVB	Temperature (°C)
January	179.04	39.05	4	12.54
February	90.39	30.94	4	14.14
March	211.37	34.16	5	15.89
April	148.61	24.27	5	17.86
May	141.93	39.05	5	12.54
June	162.83	25.75	5	20.74
July	193.67	64.52	4	17.70
August	174.82	61.17	4	18.57
September	168.56	71.65	4	17.84
October	106.56	60.74	4	17.16
November	62.55	37.49	3	15.94
December	114.70	48.56	3	11.93

Table 3 Monthly average of the year 2017 of diffuse radiation, relative humidity uvb index and temperature
Own Elaboration

Month	Diffuse radiation (W/m²)	Relative Humidity (%)	UVVB	Temperature (°C)
January	101.47	42.92	3	11.77
February	145.77	49.84	4	14.56
March	86.74	24.98	5	17.57
April	143.78	28.71	3	18.18
May	133.49	42.92	3	11.77
June	162.57	39.85	2	18.06
July	174.32	54.26	2	18.57
August	155.91	59.81	2	18.07
September	185.86	76.31	3	17.67
October	161.07	68.76	4	15.88
November	159.30	55.68	2	13.72

Table 4 Monthly average of the year 2017 of diffuse radiation, relative humidity uvb index and temperature
Own Elaboration

Tables 3 and 4 show the monthly averages of diffuse radiation, relative humidity, UVV index and temperature for different months of the year. Table 1 shows that diffuse radiation has the highest values in January, March, June, July and August, while the months with the lowest diffuse radiation are February, April, May, October, November and December. Relative humidity is highest in September and lowest in April. The UVB index remains constant at 4 for most of the year, while in March and April it is 5. The highest average temperatures are recorded in June and the lowest in January.

On the other hand, table 4 shows that scattered radiation has higher values in February, September and October, while the months with the lowest scattered radiation are March, April and November. Relative humidity is highest in September and lowest in March. The UVB index has a value of 3 in March, April, July, August and November, while in the rest of the months it has a value of 2 or 4. The highest average temperature is observed in August and the lowest in November.

Thus, both tables provide valuable information on the monthly changes of the measured parameters in 2017 and 2018. These data can be used for a more detailed and comprehensive analysis in the future.

Variable 1	Variable 2	Correlation	Correlation type	Acceptable
Diffuse Radiation (W/m²)	UVVB	0.4511945	Positive	Yes
	Temperature (°C)	0.2877612	Positive	Yes
	Relative Humidity (%)	0.1791565	Positive	Yes
UVVB	Diffuse Radiation(W/m²)	0.4511945	Positive	Yes
	Temperature (°C)	0.4497433	Positive	Yes
	Relative Humidity (%)	-0.3198623	Negative	Yes
Temperature (°C)	Diffuse Radiation(W/m²)	0.2877612	Positive	Yes
	UVVB	0.4497433	Positive	Yes
	Relative Humidity (%)	0.0498341	Positive	No
Relative Humidity (%)	Diffuse Radiation(W/m²)	0.1791565	Positive	Yes
	UVVB	-0.3198623	Negative	Yes
	Temperature (°C)	0.0498341	Positive	No

Table 5 Correlation of the data in table 3
Own Elaboration

Variable 1	Variable 2	Correlation	Type of correlation	Acceptable
Diffuse radiation (W/m²)	UVVB	0.4511945	Positive	Yes
	Temperature (°C)	0.2877612	Positive	Yes
	Relative humidity (%)	0.1791565	Positive	Yes
	Diffuse radiation (W/m²)	0.4511945	Positive	Yes
UVVB	Temperaturae(°C)	0.4497433	Positive	Yes
	Relative humidity (%)	-0.3198623	Negative	Yes
Temperature (°C)	Diffuse Radiation (W/m²)	0.2877612	Positive	Yes
	UVVB	0.4497433	Positive	Yes
	Humidity relative (%)	0.0498341	Positive	No
Relative humidity (%)	Diffuse radiation (W/m²)	0.1791565	Positive	Yes
	UVVB	-0.3198623	Negative	Yes
	Temperature (°C)	0.0498341	Positive	No

Table 6 Correlation of the data in table 4
Own Elaboration

Tables 5 and 6 above show the results of correlations obtained with the R code, which is shown in the annex, both tables present the results of the Pearson correlation of the data for diffuse radiation, UVB, temperature and relative humidity. Pearson's correlation is a measure of the linear relationship between two variables, ranging from -1 to 1, while a value close to -1 indicates a strong positive correlation, while a value close to -1 indicates a positive correlation. In both tables, diffuse radiation and UVB have a strong positive correlation. In addition, temperature and relative humidity are also positively correlated, although to a lesser extent.

ISSN 2524-2121

On the other hand, in table 5, a negative correlation is observed between relative humidity and UVB, indicating that as humidity increases, UVB intensity decreases. However, in table 6, the correlation between relative humidity and UVB is not significant.

In general, these tables indicate the relationship between the variables measured in the study and may be useful to better understand how these variables are related in the region and how they may affect biological and ecological processes in the area.

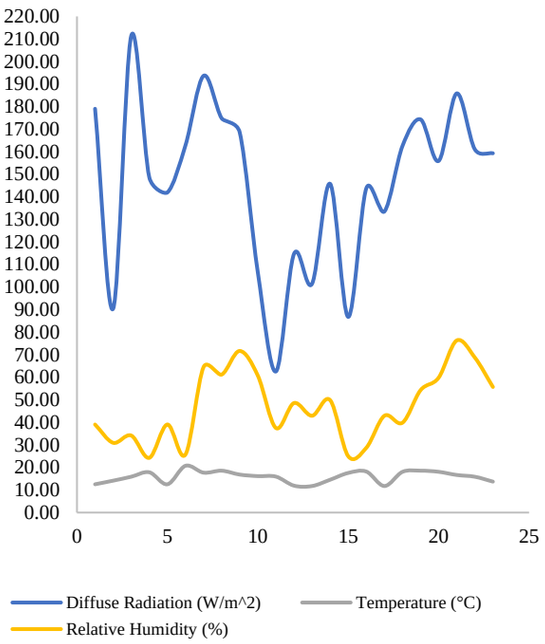

Graph 1 Comparison of diffuse radiation, relative humidity and temperature from 2017 to 2018
Own Elaboration

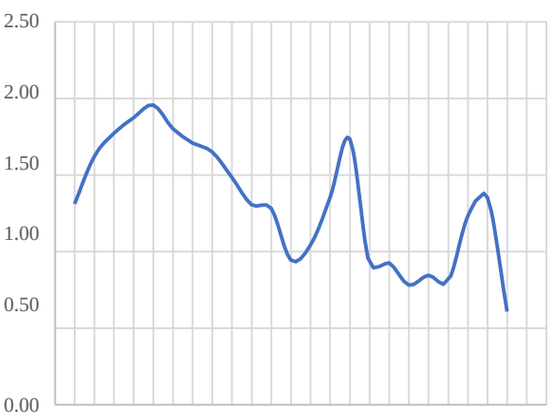

Graph 2 Comparison of UVB radiation from 2017 to 2018, prepared by the authors

Graph 1 shows the monthly average of diffuse radiation, temperature and humidity from 2017 to 2018, showing that in 2017 the diffuse radiation was higher than in 2018, the relative humidity was higher in 2018 and has a seasonal behaviour, i.e., depending on the time of year and climate there is more or less relative humidity and finally the temperature is the variable that has a more stable behaviour with seasonal increases and decreases.

Graph 2 shows the comparison of UVB radiation between 2017 and 2018, showing that 2017 had a higher UVB radiation compared to 2018, where there are clearly two peaks or very high increases compared to the rest of 2018.

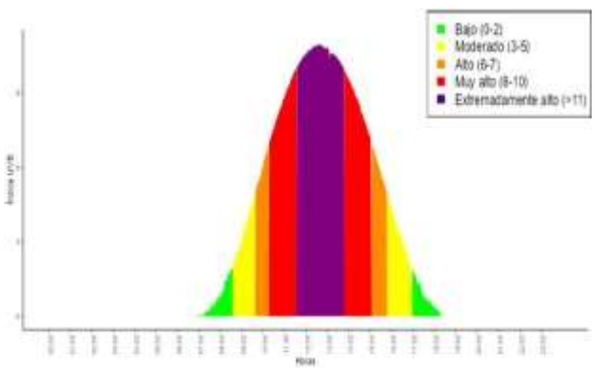

Graph 3 UVB index on 30 April 2017
Prepared by the authors

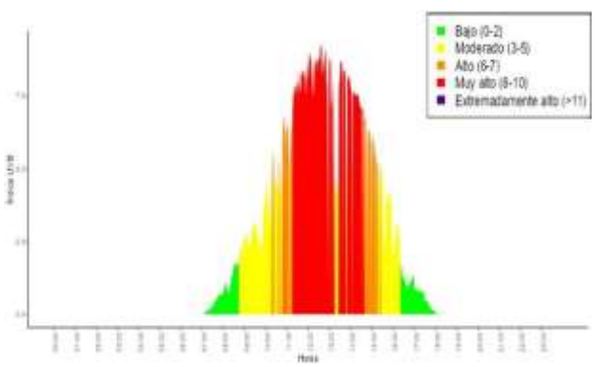

Graph 4 UVB index on the 24th of 2017, day with the highest diffuse radiation in that month
Own Elaboration

Graph 3 shows the UVB index on 30 April 2017, which shows a typical behaviour of a sunny day, with the highest UVB index at midday, while graph 4 shows the behaviour of the UVB index on 24 May, the day with the highest average diffuse radiation of that month, showing that even if there are clouds or any other pollutants in the atmosphere that cause high diffuse solar radiation, it is essential to use sun protection.

ISSN 2524-2121

Annexes

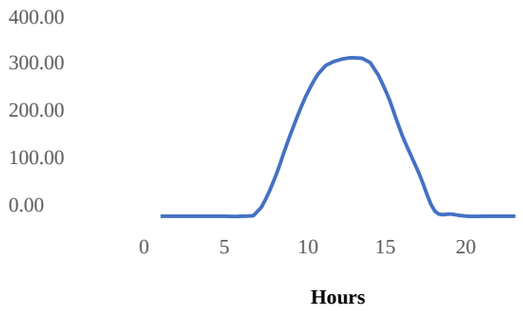

Graph 5 Diffuse solar radiation in January 2017
Prepared by the authors

Graph 5 is a sample of the more than 190 graphs made for this research where the monthly average from 2017 to 2018 for each of the variables analysed is shown.

Acknowledgements

First of all, we would like to express our sincere thanks to the Universidad Autónoma de Zacatecas for their invaluable contribution to this research. The availability and access to the solarimetric station of this institution were fundamental to carry out this study. Without their support and collaboration, this research would not have been possible.

We would also like to express our deep appreciation to the Geophysics Unit of the National Autonomous University of Mexico (UNAM) for their advice and guidance during the development of this research. Their experience and knowledge in the field of solarimetry were of great value for the interpretation of the data and the understanding of the characteristics of climate and solar radiation in the Zacatecas region.

We sincerely thank all the researchers, professors and staff of both institutions who collaborated in this project. Their commitment and dedication in the acquisition and maintenance of the measurement instruments, as well as in the management of the data, were fundamental to the success of this research.

We would also like to extend our thanks to all participants and volunteers who contributed to the data collection. Their commitment and willingness to make accurate and reliable measurements were crucial to obtain high quality results.

Finally, we would like to thank all the people who, in one way or another, contributed to this research. Their support, comments and suggestions enriched our work and motivated us to move forward in the search for scientific knowledge.

Conclusions

In conclusion, this study provided a comprehensive view of diffuse solar radiation, UV radiation, temperature and relative humidity in the study locality during 2017 and 2018. The results obtained largely supported the hypothesis by demonstrating a significant correlation between diffuse and UVB radiation with temperature and relative humidity.

The findings revealed a seasonal variability in diffuse radiation and UVB radiation, with higher values in the summer and autumn months. Temperature and relative humidity also showed seasonal patterns, with peaks in May and September. These relationships between the parameters studied provide valuable information for solar energy system design, outdoor event planning and climate change analysis.

The results may also be useful in urban planning and agriculture, as information on solar radiation and temperature can guide building energy efficiency and occupant comfort, while UVB radiation and relative humidity can influence sun protection measures and irrigation in agriculture.

In summary, this study provides a solid basis for future research in the field of solar energy, climatology and climate change. The data and conclusions obtained are relevant for various applications and contribute to scientific knowledge in the area.

References

[I] Loachamín, J., & Gabriel, W. (2014).Análisis y modelamiento del impacto de la radiación difusa en la generación eléctrica usando paneles solares fotovoltaicos policristalinos.

ISSN 2524-2121

[II] Martínez, R. I. P. ., Ortega, D. J. P. ., Velazco, C. A. R. ., Alomia, F. A. B. ., Paredes, E. D. O. ., & Medina, J. D. C. . (2022). Determinación del nivel de riesgo ocupacional por exposición a la radiación ultravioleta de origen solar en oficinas - estudio de caso en Pasto Colombia. South American SciencesISSN 2675-7222, 3(1), e22171. https://doi.org/10.52755/sas.v3i1.171

[III] Angeles Vásquez, R., García Corzo, A., & Angeles Suazo, J. . (2021). Gradiente altitudinal de la radiación ultravioleta en la región Junín rospectiva niversitaria, 18(1) 47–51. https://doi.org/10.26490/uncp.prospectivauniversitaria.2021.18.1415

[IV] López de la Fuente, J. (1998). La temperatura ambiental en Managua y el efecto invernadero, 1989-1998. Encuentro, 46, 3–15. https://doi.org/10.5377/encuentro.v0i46.3752

[V] Rojas Carrizales, A., Torres Gonzales,Y., Parejas Garavito, M., & HinojosaBenavides, R. (2021). Acción del agua y la temperatura ambiental extrema sobre pavimento flexible. GnosisWisdom, 2, 39–48. https://doi.org/10.54556/gnosiswisdom. v1i2.17

[VI] Cainzos, R. P., Koscinczuk, P., &Ferreiro, M. C. (2016). Influencia de la temperatura ambiental sobre la presión arterial del perro. Revista Veterinaria, 2, 154. https://doi.org/10.30972/vet.252510

[VII] Borbolla Gaxiola, C. (2021). Importancia del análisis del comportamiento higrotérmico de inmuebles históricos para la rehabilitación energética. Caso del archivo histórico general del estado de Sinaloa. Contexto, 22. https://doi.org/10.29105/contexto15.22-4

ISSN 2524-2121

[Title in Times New Roman and Bold No. 14 in English and Spanish]

Surname (IN UPPERCASE), Name 1st Author†*, Surname (IN UPPERCASE), Name 1st Coauthor, Surname (IN UPPERCASE), Name 2nd Coauthor and Surname (IN UPPERCASE), Name 3rd Coauthor

Institutional Affiliation of Author including Dependency (No.10 Times New Roman and Italic)

International Identification of Science - Technology and Innovation

ID 1st Author: (ORC ID - Researcher ID Thomson, arXiv Author ID - PubMed Author ID - Open ID) and CVU 1st author: (Scholar-PNPC or SNI-CONAHCYT) (No.10 Times New Roman)

ID 1st Coauthor: (ORC ID - Researcher ID Thomson, arXiv Author ID - PubMed Author ID - Open ID) and CVU 1st coauthor: (Scholar or SNI) (No.10 Times New Roman)

ID 2nd Coauthor: (ORC ID - Researcher ID Thomson, arXiv Author ID - PubMed Author ID - Open ID) and CVU 2nd coauthor: (Scholar or SNI) (No.10 Times New Roman)

ID 3rd Coauthor: (ORC ID - Researcher ID Thomson, arXiv Author ID - PubMed Author ID - Open ID) and CVU 3rd coauthor: (Scholar or SNI) (No.10 Times New Roman)

(Report Submission Date: Month, Day, and Year); Accepted (Insert date of Acceptance: Use Only ECORFAN)

Abstract (In English, 150-200 words)

Objectives
Methodology
Contribution

Abstract (In Spanish, 150-200 words)

Objectives
Methodology
Contribution

Keywords (In English)

Indicate 3 keywords in Times New Roman and Bold No. 10

Keywords (In Spanish)

Indicate 3 keywords in Times New Roman and Bold No. 10

Citation: Surname (IN UPPERCASE), Name 1st Author, Surname (IN UPPERCASE), Name 1st Coauthor, Surname (IN UPPERCASE), Name 2nd Coauthor and Surname (IN UPPERCASE), Name 3rd Coauthor. Paper Title. ECORFAN Journal-Taiwan. Year 1-1: 1-11 [Times New Roman No.10]

* Correspondence to Author (example@example.org)
† Researcher contributing as first author.

Introduction

Text in Times New Roman No.12, single space.

General explanation of the subject and explain why it is important.

What is your added value with respect to other techniques?

Clearly focus each of its features

Clearly explain the problem to be solved and the central hypothesis.

Explanation of sections Article.

Development of headings and subheadings of the article with subsequent numbers

[Title No.12 in Times New Roman, single spaced and bold]

Products in development No.12 Times New Roman, single spaced.

Including graphs, figures and tables-Editable

In the article content any graphic, table and figure should be editable formats that can change size, type and number of letter, for the purposes of edition, these must be high quality, not pixelated and should be noticeable even reducing image scale.

[Indicating the title at the bottom with No.10 and Times New Roman Bold]

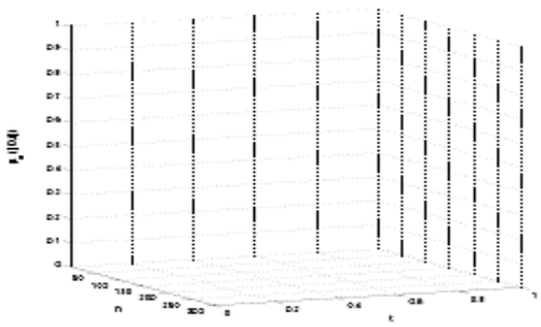

Graphic 1 Title and *Source (in italics)*

Should not be images-everything must be editable.

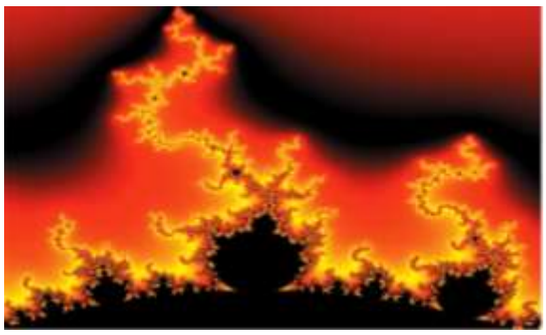

Figure 1 Title and *Source (in italics)*

Should not be images-everything must be editable.

Table 1 Title and *Source (in italics)*

Should not be images-everything must be editable.

Each article shall present separately in **3 folders**: a) Figures, b) Charts and c) Tables in .JPG format, indicating the number and sequential Bold Title.

For the use of equations, noted as follows:

$$Y_{ij} = \alpha + \sum_{h=1}^{r} \beta_h X_{hij} + u_j + e_{ij} \qquad (1)$$

Must be editable and number aligned on the right side.

Methodology

Develop give the meaning of the variables in linear writing and important is the comparison of the used criteria.

Results

The results shall be by section of the article.

Annexes

Tables and adequate sources

Thanks

Indicate if they were financed by any institution, University or company.

Conclusions

Explain clearly the results and possibilities of improvement.

ISSN 2524-2121

References

Use APA system. Should not be numbered, nor with bullets, however if necessary numbering will be because reference or mention is made somewhere in the Article.

Use Roman Alphabet, all references you have used must be in the Roman Alphabet, even if you have quoted an Article, book in any of the official languages of the United Nations (English, French, German, Chinese, Russian, Portuguese, Italian, Spanish, Arabic), you must write the reference in Roman script and not in any of the official languages.

Technical Specifications

Each article must submit your dates into a Word document (.docx):

Journal Name
Article title
Abstract
Keywords
Article sections, for example:

1. Introduction
2. Description of the method
3. Analysis from the regression demand curve
4. Results
5. Thanks
6. Conclusions
7. References

Author Name (s)
Email Correspondence to Author
References

Intellectual Property Requirements for editing:

-Authentic Signature in Color of Originality Format Author and Coauthors

-Authentic Signature in Color of the Acceptance Format of Author and Coauthors

- Authentic Signature in Color of the Conflict of Interest Format of Author and Co-authors.

ISSN 2524-2121

Reservation to Editorial Policy

ECORFAN Journal-Taiwan reserves the right to make editorial changes required to adapt the Articles to the Editorial Policy of the Journal. Once the Article is accepted in its final version, the Journal will send the author the proofs for review. ECORFAN® will only accept the correction of errata and errors or omissions arising from the editing process of the Journal, reserving in full the copyrights and content dissemination. No deletions, substitutions or additions that alter the formation of the Article will be accepted.

Code of Ethics - Good Practices and Declaration of Solution to Editorial Conflicts

Declaration of Originality and unpublished character of the Article, of Authors, on the obtaining of data and interpretation of results, Acknowledgments, Conflict of interests, Assignment of rights and Distribution.

The ECORFAN-Mexico, S.C Management claims to Authors of Articles that its content must be original, unpublished and of Scientific, Technological and Innovation content to be submitted for evaluation.

The Authors signing the Article must be the same that have contributed to its conception, realization and development, as well as obtaining the data, interpreting the results, drafting and reviewing it. The Corresponding Author of the proposed Article will request the form that follows.

Article title:

– The sending of an Article to ECORFAN Journal- Taiwan emanates the commitment of the author not to submit it simultaneously to the consideration of other series publications for it must complement the Format of Originality for its Article, unless it is rejected by the Arbitration Committee, it may be withdrawn.

– None of the data presented in this article has been plagiarized or invented. The original data are clearly distinguished from those already published. And it is known of the test in PLAGSCAN if a level of plagiarism is detected Positive will not proceed to arbitrate.

– References are cited on which the information contained in the Article is based, as well as theories and data from other previously published Articles.

– The authors sign the Format of Authorization for their Article to be disseminated by means that ECORFAN-Mexico, S.C. In its Holding Taiwan considers pertinent for disclosure and diffusion of its Article its Rights of Work.

– Consent has been obtained from those who have contributed unpublished data obtained through verbal or written communication, and such communication and Authorship are adequately identified.

– The Author and Co-Authors who sign this work have participated in its planning, design and execution, as well as in the interpretation of the results. They also critically reviewed the paper, approved its final version and agreed with its publication.

– No signature responsible for the work has been omitted and the criteria of Scientific Authorization are satisfied.

– The results of this Article have been interpreted objectively. Any results contrary to the point of view of those who sign are exposed and discussed in the Article.

Copyright and Access

The publication of this Article supposes the transfer of the copyright to ECORFAN-Mexico, SC in its Holding Taiwan for its ECORFAN Journal- Taiwan, which reserves the right to distribute on the Web the published version of the Article and the making available of the Article in This format supposes for its Authors the fulfilment of what is established in the Law of Science and Technology of the United Mexican States, regarding the obligation to allow access to the results of Scientific Research.

Article Title:

Name and Surnames of the Contact Author and the Coauthors	Signature
1.	
2.	
3.	
4.	

Principles of Ethics and Declaration of Solution to Editorial Conflicts

Editor Responsibilities

The Publisher undertakes to guarantee the confidentiality of the evaluation process, it may not disclose to the Arbitrators the identity of the Authors, nor may it reveal the identity of the Arbitrators at any time.

The Editor assumes the responsibility to properly inform the Author of the stage of the editorial process in which the text is sent, as well as the resolutions of Double-Blind Review.
The Editor should evaluate manuscripts and their intellectual content without distinction of race, gender, sexual orientation, religious beliefs, ethnicity, nationality, or the political philosophy of the Authors.

The Editor and his editing team of ECORFAN® Holdings will not disclose any information about Articles submitted to anyone other than the corresponding Author.

The Editor should make fair and impartial decisions and ensure a fair Double-Blind Review.

Responsibilities of the Editorial Board

The description of the peer review processes is made known by the Editorial Board in order that the Authors know what the evaluation criteria are and will always be willing to justify any controversy in the evaluation process. In case of Plagiarism Detection to the Article the Committee notifies the Authors for Violation to the Right of Scientific, Technological and Innovation Authorization.

Responsibilities of the Arbitration Committee

The Arbitrators undertake to notify about any unethical conduct by the Authors and to indicate all the information that may be reason to reject the publication of the Articles. In addition, they must undertake to keep confidential information related to the Articles they evaluate.

Any manuscript received for your arbitration must be treated as confidential, should not be displayed or discussed with other experts, except with the permission of the Editor.

The Arbitrators must be conducted objectively, any personal criticism of the Author is inappropriate.

The Arbitrators must express their points of view with clarity and with valid arguments that contribute to the Scientific, Technological and Innovation of the Author.

The Arbitrators should not evaluate manuscripts in which they have conflicts of interest and have been notified to the Editor before submitting the Article for Double-Blind Review.

Responsibilities of the Authors

Authors must guarantee that their articles are the product of their original work and that the data has been obtained ethically.

Authors must ensure that they have not been previously published or that they are not considered in another serial publication.

Authors must strictly follow the rules for the publication of Defined Articles by the Editorial Board.

The authors have requested that the text in all its forms be an unethical editorial behavior and is unacceptable, consequently, any manuscript that incurs in plagiarism is eliminated and not considered for publication.

Authors should cite publications that have been influential in the nature of the Article submitted to arbitration.

Information services

Indexation - Bases and Repositories

RESEARCH GATE (Germany)
GOOGLE SCHOLAR (Citation indices-Google)
MENDELEY (Bibliographic References Manager)
HISPANA (Information and Bibliographic Orientation-Spain)

Publishing Services

Citation and Index Identification H
Management of Originality Format and Authorization
Testing Article with PLAGSCAN
Article Evaluation
Certificate of Double-Blind Review
Article Edition
Web layout
Indexing and Repository
ArticleTranslation
Article Publication
Certificate of Article
Service Billing

Editorial Policy and Management

69 Street. YongHe district, ZhongXin. Taipei-Taiwan. Phones: +52 1 55 6159 2296, +52 1 55 1260 0355, +52 1 55 6034 9181; Email: contact@ecorfan.org www.ecorfan.org

ECORFAN Journal-Taiwan

2524-2121
ISSN 2524-2121
www.ecorfan.org